

# MAGNETISM AND ELECTRONIC TRANSPORT PROPERTIES IN CARBON NANOTUBE HETEROJUNCTIONS

## Dissertation

Submitted in partial fulfillment of the requirements  
for the degree of  
**Master of Science**

*by*  
**Dwaipayan Paul**

1811064

*Supervised by*  
**Dr. Joydeep Bhattacharjee**



*to the*  
**School of Physical Sciences**  
**National Institute of Science Education and Research,**  
**Bhubaneswar**  
**Date: 27.11.2022**

*Dedicated to my parents*

## **DECLARATION**

I hereby declare that I am the sole author of this thesis in partial fulfillment of the requirements for a postgraduate degree from National Institute of Science Education and Research (NISER). I authorize NISER to lend this thesis to other institutions or individuals for the purpose of scholarly research.

Signature of the Student

Date:

The thesis work reported in the thesis entitled "*Magnetism and Electronic Transport properties in Carbon Nanotube Heterojunctions*" was carried out under my supervision, in the *School of Physical Sciences* at NISER, Bhubaneswar, India.

Signature of the thesis supervisor

School:

Date:

## **ACKNOWLEDGEMENTS**

Firstly, I would like to thank my supervisor Dr. Joydeep Bhattacharjee for being a great and valuable support for me.

I am grateful to all seniors in the office, my lab members specially Sujith Da who constantly helped me through my doubts and lack of theoretical knowledge.

I would like to express my special thanks to the faculty of School of Physical Sciences, NISER for giving me the opportunity and tools needed for this project.

My heartfelt thanks to some of my close friends for their endless support, and motivational words, which made this journey a lot easier.

## ABSTRACT

Iijima's discovery of carbon nanotubes(CNTs) opened the door to their potential usage as electrical components in a range of nano-scale gadgets. Its distinctive property—that its band gap, which ranges from that of a metal to that of a semiconductor—depends on structural orientation or chirality—attracted the attention of researchers. That indicates that a CNT can be grown into a metal or a semiconductor by altering the conditions of its growth.

This project is about predicting a linear carbon nanotube heterojunction (CNT-HJ) suitable for device applications by studying its magnetic and transport properties. We proceeded with relaxation study, which is important to predict linear carbon nanotube heterojunctions which are more favourable for device applications. A systematic magnetism study showed a relationship between defects and ferromagnetic behaviour. We continued our investigation by finding the density of states(DOS) in CNT-HJs using the tight-binding approximation. A few carbon nanotube heterojunctions (CNT-HJs) of metal-semiconductor(MS) and semiconductor-semiconductor(SS) types showed defect states appearing near the Fermi level in the DOS plots. An extensive transport study needed to be done to justify that the defect states are isolated(non-contributing in zero-bias condition) and become a channel between two nanotubes when a bias is applied.

Overall, this study adds to our understanding of carbon nanotube heterojunction properties and prospective applications. The discoveries add to the expanding field of nanoelectronics and pave the way for the design and production of innovative devices with improved functionality and energy efficiency.

# Contents

<b>1</b>	<b>Introduction</b>	<b>1</b>
1.1	Structural properties of Carbon nanotubes . . . . .	3
1.2	Interfacing CNTs: CNT heterojunctions . . . . .	5
1.3	Limitations on forming a heterojunction . . . . .	10
<b>2</b>	<b>Structural Optimisation</b>	<b>12</b>
2.1	Classical relaxation using molecular dynamics . . . . .	12
2.2	Bending angle of a relaxed heterojunction . . . . .	13
2.3	Results . . . . .	15
<b>3</b>	<b>Electronic structure theory</b>	<b>18</b>
3.1	Tight Binding Model . . . . .	18
3.2	Hubbard Model . . . . .	24
3.3	Mean Field approximation . . . . .	25
3.4	Results . . . . .	27
3.4.1	Magnetic CNT HJs . . . . .	27
3.4.2	Projected DOS on tube axis . . . . .	35
<b>4</b>	<b>Electronic transport theory</b>	<b>40</b>
4.1	Non-equilibrium Green's function formalism . . . . .	40
4.1.1	Contact-channel coupling . . . . .	40
4.1.2	Green's function calculation . . . . .	44
4.1.3	Green's function convergence . . . . .	45
4.1.4	Zero bias transport . . . . .	46
4.1.5	Zero bias Transmission function . . . . .	48
4.2	Results . . . . .	49
4.2.1	Transmission function in MS and SS heterojunctions . . . . .	49
4.2.2	Isolated defect states . . . . .	51
<b>5</b>	<b>Conclusion</b>	<b>57</b>

# List of Figures

1.1	Depiction of folding graphene to make a CNT with the chiral vector $\mathbf{R}$ as the tube axis . . . . .	4
1.2	Zigzag type Carbon nanotube (9,0) . . . . .	4
1.3	Armchair type Carbon nanotube (5,5) . . . . .	4
1.4	Chiral type tube (10,5) . . . . .	5
1.5	(a) Two different CNTs of similiar radius . . . . .	6
1.6	(b) Unwinding of CNTs, showing characteristic triangles ABC and A'B'C . . . . .	6
1.7	(C) Quadrangle ABA'C will be formed at the interface . . . . .	6
1.8	. . . . .	6
1.9	(i) Heterojunction with different numbers of topological defects . . . . .	8
1.10	(ii) Energy-minimized structures corresponding to above configurations . . . . .	8
1.11	. . . . .	8
1.12	The building blocks for interfacing the graphene nanoribbons . . . . .	8
1.13	Interfacing (10,8) and (12,6) . . . . .	9
2.1	(a) Minimum strain in case of three hexagons (b) Pentagon defect stretches two hexagons (c) Heptagon defect compresses two hexagons . . . . .	14
2.2	(a) and (c) regions are the edges of the CNTs, (b) region is the heterojunction; (1), (2) and (3) are center of masses of the regions (a), (b) and (c) . . . . .	14
2.3	1 A type defect(7,6-7,6); $\phi = 8.146$ deg . . . . .	15
2.4	2 A type defect(uniform) (10,4-6,8); $\phi = 0.01$ deg . . . . .	16
2.5	2 A type defect(lumped) (10,4-6,8); $\phi = 13.017$ deg . . . . .	16
2.6	3 A type defect(uniform) (11,8-11,8); $\phi = 2.07$ deg . . . . .	16
2.7	1 B type defect (2,12-13,0); $\phi = 9.83$ deg . . . . .	17
2.8	1 B and 1 A type defect (12,2-5,10); $\phi = 4.413$ deg . . . . .	17
3.1	Edges showed by bold line: (a) Zig-zag type edges, (b) Armchair type edges . . . . .	27
3.2	Visualisation of spin charge densities . . . . .	28
3.3	(10,4-6,8) HJ . . . . .	31
3.4	{(6,9-12,2)} HJ . . . . .	31
3.5	(13,0-6,9) HJ . . . . .	31
3.6	(2,12-13,0) HJ . . . . .	32
3.7	{(10,5-8,6)} HJ . . . . .	32
3.8	(12,2-5,10) HJ . . . . .	32
3.9	(6,9-10,4) HJ . . . . .	33
3.10	PDOS of (Blue) Tube 1; (Red) Junctions; (Green) Tube 2 . . . . .	35
3.11	<b>(10,4-6,8)</b> HJ (a) Length: 15 Ang; (b) Length: 25 Ang; (c) Length: 35 Ang . . . . .	36
3.12	<b>(6,9-12,2)</b> HJ (a) Length: 15 Ang; (b) Length: 25 Ang; (c) Length: 35 Ang . . . . .	36
3.13	<b>(13,0-6,9)</b> HJ (a) Length: 15 Ang; (b) Length: 25 Ang; (c) Length: 35 Ang . . . . .	37
3.14	Energy diagram with respect to distance, for <b>(13,0-6,9)</b> HJ . . . . .	37

*LIST OF FIGURES*

---

3.15 <b>(2,12-13,0)</b> HJ (a) Length: 15 Ang; (b) Length: 25 Ang; (c) Length: 35 Ang . . . . .	38
3.16 <b>(12,2-5,10)</b> HJ (a) Length: 15 Ang; (b) Length: 25 Ang; (c) Length: 35 Ang . . . . .	38
3.17 <b>(10,5-8,6)</b> HJ (a) Length: 15 Ang; (b) Length: 25 Ang; (c) Length: 35 Ang . . . . .	39
3.18 Energy diagram with respect to distance, for <b>(10,5-8,6)</b> HJ . . . . .	39
4.1 Channel coupled to a single contact[1] . . . . .	40
4.2 Channel coupled to source and drain[1] . . . . .	42
4.3 Two principal layers constructed at an edge of CNT . . . . .	46
4.4 Inflow and outflow at the contacts[1] . . . . .	48
4.5 (a) 10,4-6,8 ( <b>2A type</b> ) (b) 6,9-12,2 ( <b>2A+1B type</b> ) (c) 13,0-6,9 ( <b>2A+2B type</b> ) . . . . .	50
4.6 (a) 2,12-13,0 ( <b>1B type</b> ) (b) 12,2-5,10 ( <b>1A+1B type</b> ) (c) 10,5-8,6 ( <b>2A+1B type</b> ) . . . . .	50
4.7 6,7 - 9,4 ; Radius = 4 Ang. . . . .	51
4.8 10,5 - 7,8 ; Radius = 5 Ang. . . . .	52
4.9 11,6 - 8,9 ; Radius = 6 Ang. . . . .	52
4.10 9,5 - 8,6 ; Radius = 5 Ang. . . . .	52
4.11 11,6 - 9,8 ; Radius = 6 Ang. . . . .	53
4.12 13,8 - 11,10 ; Radius = 7 Ang. . . . .	53
4.13 8,4 - 8,4 ; Radius = 4 Ang. . . . .	53
4.14 12,5 - 9,8 ; Radius = 6 Ang. . . . .	54
4.15 13,5 - 10,8 ; Radius = 6 Ang. . . . .	54
4.16 10,5 - 8,6 ; Radius = 5 Ang. . . . .	54
4.17 14,3 - 7,11 ; Radius = 6 Ang. . . . .	55
4.18 DOS of pristine tubes and the heterojunction (10,5-7,8) . . . . .	56
5.1 Device applications of linear MS and SS heterojunctions . . . . .	58

# Chapter 1

## Introduction

With discovery of carbon nanotubes by Iijima[2], it showed a possible way to be used as electrical components in variety of nano-scale devices. It attracted the attention of researchers due to its unique property which is, its band gap(varied from that of a metal to a semiconductor) depends on structural orientation or its chirality. That means, a CNT can be grown into a metal or a semiconductor by changing its growth conditions(still not realised experimentally). However, it is feasible to develop or join two CNTs with different chiralities to form a heterojunction, a 0-D sp<sub>2</sub>-bonded nanoscale interface.

Due to the rarity of CNT HJs in nature and the fundamental difficulties involved in conducting simultaneous structural characterization and electrical measurements at nm length scales, this class of nanoscale interfaces have not yet been thoroughly investigated. The simplest topological defects that can exist in graphene without causing dangling bonds are interfacial pentagons and heptagons, which were previously discovered in CNT-HJs using scanning tunnelling microscopy[3]. Although it was known that a pair of these topological defects can be utilised to connect two CNTs with different chiralities (with relatively same radius)[4], earlier theory has shown that the number and arrangement of these defects can have a significant impact on the electrical properties of the connected CNTs. However, it is not fully known what physical parameters are affected, and how those structural characteristics relate to the possible functionality of the device.

There aren't many controlled synthesis techniques available for CNT heterojunctions.

However, developments in CNT-HJ synthesis showed that changing the temperature during chemical vapour deposition can change chirality during growth[5]. It has also been shown that current-induced annealing can directly fuse two CNTs with different chiralities[6]. Rayleigh scattering-based techniques can be used to determine constituent chiralities. When combined with precise electrical transport measurements through CNT-HJs, it would enable a systematic understanding of relationships between structure and electronic properties of single-walled CNT-HJ devices.

This thesis project gives a computational investigation of carbon nanotube heterojunctions using electrical transport theory in tight-binding basis. The study focuses on the characterisation of these heterojunctions in order to find possible applications in active on/off devices. The spin-polarized (in tight binding) analysis results revealed the presence of magnetic behaviour in certain carbon nanotube heterojunction and their dependence on the number and type of defects. This magnetic behaviour opens up new prospects for using these heterojunctions in memory devices (they can be used for data storage). The DOS study showed energy levels around the Fermi level in certain heterojunctions. These energy states were discovered to result from physical defects in the carbon nanotube heterojunctions- pentagons and heptagons (section 1.2). This discovery opens the door to the construction of on/off devices and possibly rectifiers if the CNTs are doped. These rectifiers have the potential to revolutionize electronics by allowing the fabrication of active and passive circuit parts with negligible Joule heating.

## 1.1 Structural properties of Carbon nanotubes

Carbon nanotubes (CNTs) (here single-walled carbon nanotubes or SWCNTs) are formed by folding the graphene sheets into a cylindrical structure, along one of its two-dimensional lattice vectors

$$\mathbf{R} = \mathbf{R}_1 + \mathbf{R}_2$$

where  $\mathbf{R}_1$  and  $\mathbf{R}_2$  are primitive lattice vectors of graphene and  $\mathbf{R}$  is called the chiral vector. Let us say we form a carbon nanotube with circumference  $|\mathbf{R}|$  and chirality  $(n,m)$ , which will have a diameter  $d$  and chiral angle  $\theta$

$$d = \frac{|\mathbf{R}|}{\pi}$$

where  $|\mathbf{R}| = \sqrt{3}a_c\sqrt{n^2 + nm + m^2}$ ,  $a_c$  is the C-C bond length which is typically 1.42 Å.

$$\theta = \tan^{-1} \left( \frac{\sqrt{3}m}{2n+m} \right)$$

This is depicted in figure 1.4, the chiral vector OB which is the tube axis,

$$OB = n\mathbf{R}_1 + m\mathbf{R}_2$$

The length of the chiral vector is the circumference of the tube. The structure of a carbon nanotube is defined by its chirality  $(n,m)$ , which is unique for a tube. Although the basic shape of all carbon nanotubes is cylindrical, the orientation of hexagons (in graphite sheet) relative to the axis of the CNTs is different for different chiralities. This results in a change in the electronic properties of CNTs.

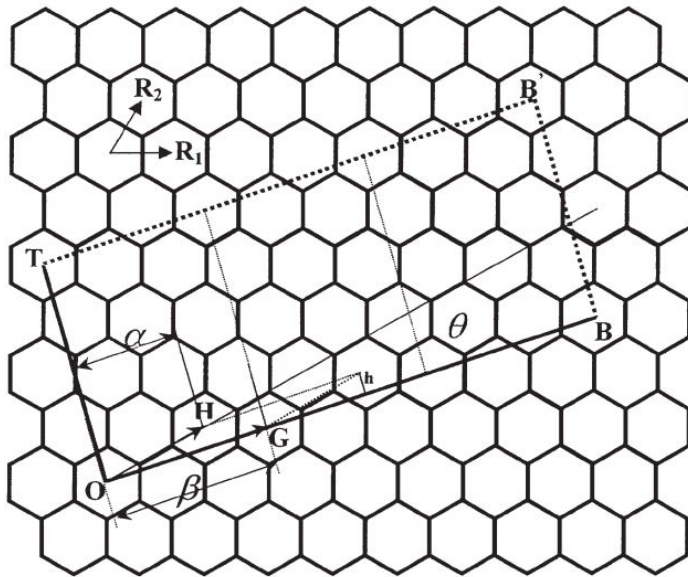


Figure 1.1: Depiction of folding graphene to make a CNT with the chiral vector  $\mathbf{R}$  as the tube axis

The tubes can be classified in terms of chiral angle  $\theta$  which is defined as the angle between the tube circumference and the nearest zig-zag of C-C bonds,

- Zigzag type carbon nanotubes: For  $\theta = 0$ , chiralities of the form  $(m,0)$ .
- Armchair type carbon nanotubes: For  $\theta = \frac{\pi}{6}$ , chiralities of the form  $(m,m)$ .
- Chiral type carbon nanotubes: For  $0 < \theta < \frac{\pi}{6}$ .

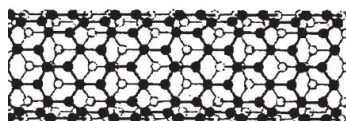


Figure 1.2: Zigzag type Carbon nanotube (9,0)

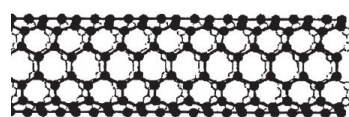


Figure 1.3: Armchair type Carbon nanotube (5,5)

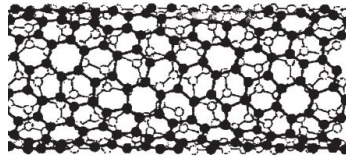


Figure 1.4: Chiral type tube (10,5)

In terms of electronic structure, it is found that all (n,m) CNTs are metallic (or very low band gap) when n-m is divisible by 3. However for CNTs with low radius, this description fails due to the high curvature effects. In this report, we will consider the above description to be correct.

The one-dimensional translational vector  $\mathbf{T}$  shown in Fig. 1.4 is defined to be the unit vector of a carbon nanotube, which is parallel to the tube axis and is normal to chiral vector  $\mathbf{R}$ . We can express  $\mathbf{T}$  as  $\mathbf{T} = t_1 \mathbf{R}_1 + t_2 \mathbf{R}_2$ , where  $t_1$  and  $t_2$  are integers.

Using  $\mathbf{R} \times \mathbf{T} = 0$ , we get,

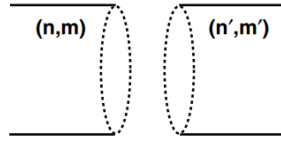
$$t_1 = \frac{2m + n}{d_R}$$

$$t_2 = -\frac{2n + m}{d_R}$$

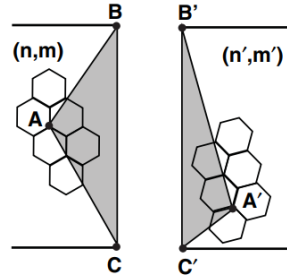
where  $d_R$  is the g.c.d of  $(2n+m, 2m+n)$ . The length of the translational vector  $\mathbf{T}$  is given by  $|\mathbf{T}| = \frac{\sqrt{3}|R|}{d_R}$ . From the figure 1.4, we see the unit cell of the CNT is the rectangle OBB'T which is defined by the chiral vector  $\mathbf{R}$  and the translational vector  $\mathbf{T}$ . The number of hexagon per unit cell  $N$  is obtained as a function of  $n$  and  $m$  as  $N = \frac{2(n^2+nm+m^2)}{d_R}$  and there are  $2N$  carbon atoms in each unit cell.

## 1.2 Interfacing CNTs: CNT heterojunctions

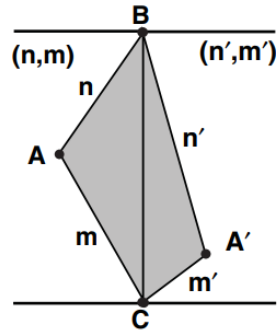
In this section, we will theoretically interface two CNTs with different chiralities using interfacial topological defects (5-7 defects or pentagons-heptagons).



(a) Two different CNTs of similar radius



(b) Unwinding of CNTs, showing characteristic triangles ABC and A'B'C'



(C) Quadrangle ABA'C will be formed at the interface

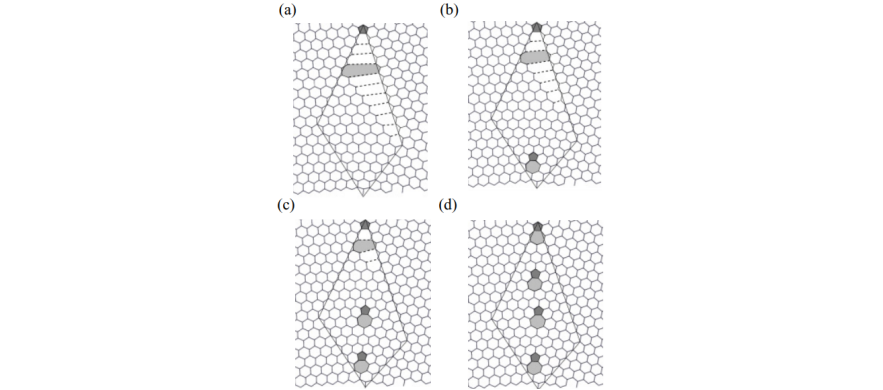
Figure 1.8

Unwinding them will give two graphene nanoribbons, hence the problem of connecting CNTs will be reduced to connecting two graphene nanoribbons at different orientations as shown in the figure 1.8 [7]. Interfacing two CNTs, say  $(n,m)$  and  $(n',m')$ , often lead to bent structure for lower number of defects. We can increase the linearity by changing the number or the arrangement of the defects. We will take an example to illustrate connecting two CNTs and then go into a general formalism.

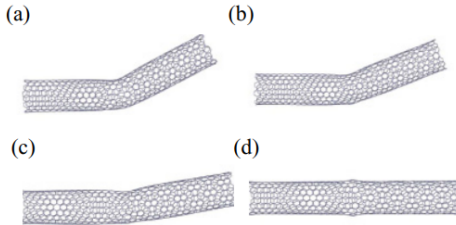
Let us take  $(10,8)$  and  $(12,6)$  CNTs for the illustration. We get the quadrangle

ABA'C, now to interface it we need identify smallest spatial regions or patches which cannot be tiled by hexagons. In this particular example (figure 1.11), we see those patches without a solid C-C bond. It is a simple case of interfacing as  $n+m=n'+m'$ , so to 'stitch' it up we need to connect a pair of atoms sequentially as shown in the figure with dashed lines. For cases where  $(n+m) \neq (n'+m')$ , we need to add  $|(n+m) - (n'+m')|$  no of extra zig-zag ridges within the patch. In figure 1.11 [i(a)], the dashed lines show strained C-C bonds. As a result of this, the two CNTs will not be collinear, as structure relaxes to reach minimum energy configuration. To make them more collinear, we have to reduce the unrealistic long C-C bonds by using more simple 5-7 defects. Figure 1.11 [i(b) to i(d)], shows that introduction of pairs of pentagons and heptagons decreases the long strained C-C bonds. With this the minimized energy structure of CNT get more linear, as we see in figure 1.11 [ii(d)], which is perfectly linear with minor protrusions and depressions around 5-7 defect sites.

Now we will go into formalising a general approach to interface CNTs with increasing linearity. Our problem here is to solve the connection in the quadrangle at the interface. To start, we take a single hexagon which can be seen as a unit quadrangle with sides say  $u, v, u', v'$  - that are similar to the indices  $n, m, n', m'$ . For a hexagon, the sides  $u, v, u', v'$  are unity as shown in the figure 1.12. It is obvious that a interface quadrangle with  $n \neq m'$  and/or  $n' \neq m$  cannot be tiled by hexagons. So we need such unit quadrangles with heptagon and pentagon, which has unequal sides. If  $(n - m') = (n' - m) > 0$ , we need such unit quadrangles whose sides follow  $(u - v') = (u' - v) = 1$ , which is the smallest unit quadrangle (figure 1.12 b). If  $(n - m') \neq (n' - m)$ , we need such unit quadrangles whose sides follow  $(u - v') \neq (u' - v)$ . The smallest such unit quadrangle will be  $(u - v') = 2, (u' - v) = 1$  (figure 3.1 c).



(i) Heterojunction with different numbers of topological defects



(ii) Energy-minimized structures corresponding to above configurations

Figure 1.11

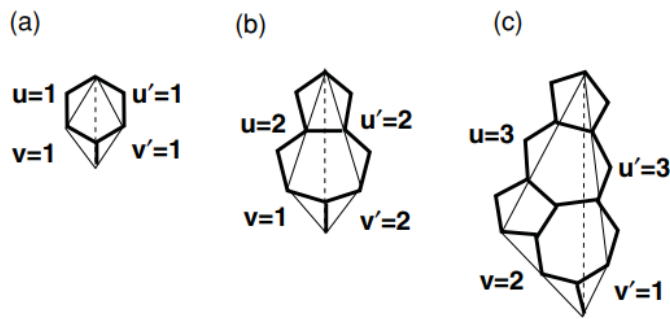


Figure 1.12: The building blocks for interfacing the graphene nanoribbons

The smallest building block which has  $(u - v') = (u' - v) = 1$  is a 5-7 defect with a single pentagon and heptagon joined together. We refer this as A-type of defect. Now the simplest building block with  $(u - v') = 2$ ,  $(u' - v) = 1$  would be two connected 5-7 defects as shown in the figure above. We refer this block as B-type defect.

Let us assume  $n \geq m'$ ,  $n' \geq m$  and  $(n-m') \geq (n'-m)$  for simplicity of our discussions.

If  $p$  and  $q$  are the minimum number numbers of B and C defect blocks inside the quadrangle, then the lengths  $(AB, CA')$  and  $(BA', AC)$  reduce in length by  $p+2q$  and  $p+q$  units of  $|\mathbf{a}|$ , where  $\mathbf{a}$  is the primitive lattice vector of graphene. Hence we get,

$$n - m' = p + 2q \quad (1.1)$$

$$n' - m = p + q \quad (1.2)$$

Thus solving the equations we get,

$$p = 2(n' - m) - (n - m') \quad (1.3)$$

$$q = (n - m') - (n' - m) \quad (1.4)$$

Total number of blocks required are  $(p + q) = n' - m$  and total number of defects is  $p + 2q = n - m'$ .

If we take an example of (10,8) and (12,6), we get  $p=4$  and  $q=0$ . Hence total number of 5-7 defects are 4.

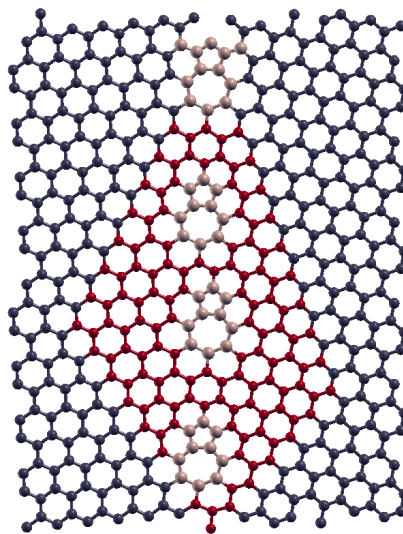


Figure 1.13: Interfacing (10,8) and (12,6)

### 1.3 Limitations on forming a heterojunction

There are a few limitations that we have to look at. The most important one is that we cannot interface two tubes if they have a significant difference in their radius. Hence, we cannot make a heterojunction with too many only A type defects because the radius gap is too much. If we want a desired number of defects which is more, we have to introduce B type defect. The second limitation is that we cannot desire for too many defects because that will lead to absurdly strained bonds and hence its classically not possible. For example: (8,0)-(7,1) should give 7 A-defects, but that will lead to strained bonds. (8,0)-(1,7) will be favoured as it has only 1 A-defect.

**(n,0)-(p,n-p)** type of heterojunctions will always give p number of A-type defects. The table below shows whether the combinations (in the range of n=6 to 11) are possible or not, based on radius difference.

Only A-type	Combinations	If possible	Only A-type	Combinations	If possible
n=6			n=7		
1 defect	(6,0)-(1,5)	yes	1 defect	(7,0)-(1,6)	yes
2 defects	(6,0)-(2,4)	no	2 defects	(7,0)-(2,5)	no
3 defects	(6,0)-(3,3)	no	3 defects	(7,0)-(3,4)	no
			4 defects	(7,0)-(4,3)	no
n=8			n=9		
1 defect	(8,0)-(1,7)	yes	1 defect	(9,0)-(1,8)	yes
2 defects	(8,0)-(2,6)	no	2 defects	(9,0)-(2,7)	yes
3 defects	(8,0)-(3,5)	no	3 defects	(9,0)-(3,6)	no
4 defects	(8,0)-(4,4)	no	4 defects	(9,0)-(4,5)	no
n=10			n=11		
1 defect	(10,0)-(1,9)	yes	1 defect	(11,0)-(1,10)	yes
2 defects	(10,0)-(2,8)	yes	2 defects	(11,0)-(2,9)	yes
3 defects	(10,0)-(3,7)	no	3 defects	(11,0)-(3,8)	no
4 defects	(10,0)-(4,6)	no	4 defects	(11,0)-(4,7)	no
5 defects	(10,0)-(5,5)	no	5 defects	(11,0)-(5,6)	no

Table 1.1: The combinations of heterojunctions which are possible only with A-type defects, based on radius difference limit.

For this range, one A-type (in case of n=6, 7 and 8) or two A-type is allowed (in case of n=9, 10 and 11) is allowed. To introduce more defects, we need B-type. The given table below demonstrates we can increase defect number with B-type defect, for (10,0) series.

No of defects	Defect type	Combinations
1 defect	(1 A)	(10,0)-(1,9)
2 defects	(2 A)	(10,0)-(2,8)
3 defects	(1 A 1 B)	(10,0)-(3,8)
4 defects	(2 A 1 B)	(10,0)-(4,7)
4 defects	(2 B)	(10,0)-(4,8)
5 defects	(3 A 1 B)	(10,0)-(5,6)
6 defects	(2 A 2 B)	(10,0)-(6,6)

Table 1.2: B-type defects to increase number of 5-7 defects in (10,0) series nanotubes

# Chapter 2

## Structural Optimisation

### 2.1 Classical relaxation using molecular dynamics

To check for strain in a system, classical relaxation is a great tool to minimise the energy of the system. For our carbon nanotube systems, we used the Brenner's potential, which is a reactive empirical potential for hydrocarbons involving bond order terms also called REBO potential.[8] The code (Brenner molecular dynamics) we used runs on Brenner potential. Additionally, we also use a Lennard-Jones potential to characterize non-bonded van der Waals interactions [9]. The total potential is given by:

$$E_{\text{pot}} = \sum_i \sum_{i < j} (V_R(r_{ij}) - \bar{B}_{ij} V_A(r_{ij}) + V_W(r_{ij}))$$

where  $r_{ij} = |\vec{x}_j - \vec{x}_i|$  denotes the distance between atoms  $i$  and  $j$ ,  $V_R$  is a pair-potential term to model the inter-atomic core-core repulsive interactions,  $V_A$  is a pair-potential term to describe the attractive interactions due to the valence electrons.  $\bar{B}_{ij}$  is called many-body empirical bond-order term which modulates valence electron densities and depends on the bond lengths and the angles.  $V_W$  denotes the contribution from the Lennard-Jones potential.

The repulsive and the attractive pair terms  $V_R$  and  $V_A$  are derived from Morse potentials and are restricted to neighbor atoms by a factor  $f(r_{ij})$ . This smoothed truncation function  $f(r_{ij})$  reads as

$$f(r_{ij}) = \begin{cases} 1 & : r_{ij} \leq R_{ij}^{(1)} \\ \frac{1}{2} \left[ 1 + \cos \left( \pi \frac{r_{ij} - R_{ij}^{(1)}}{R_{ij}^{(2)} - R_{ij}^{(1)}} \right) \right] & : R_{ij}^{(1)} \leq r_{ij} \leq R_{ij}^{(2)} \\ 0 & : r_{ij} \geq R_{ij}^{(2)} \end{cases}$$

where the cutoff parameters  $R_{ij}^{(1)}$  and  $R_{ij}^{(2)}$  only depend on the type of the atom  $i$  and  $j$  (carbon or hydrogen atoms for example). Furthermore, all terms which are used to evaluate the many-body empirical bond-order term  $\bar{B}_{ij}$  are restricted to neighbour atoms by the factor  $f$  as well. The Lennard-Jones potential  $V_W$  is defined for the contribution of the nonbonded interactions,

$$V_W(r_{ij}) = \begin{cases} 0 & : r_{ij} \leq R_{ij}^{(2)} \\ S^{(1)}(r_{ij}) & : R_{ij}^{(2)} \leq r_{ij} \leq R_{ij}^{(3)} \\ 4\epsilon_{ij} \left[ (\sigma_{ij}/r_{ij})^{12} - (\sigma_{ij}/r_{ij})^6 \right] & : R_{ij}^{(3)} \leq r_{ij} \leq R_{ij}^{(4)} \\ S^{(2)}(r_{ij}) & : R_{ij}^{(4)} \leq r_{ij} \leq R_{ij}^{(5)} \\ 0 & : r_{ij} \geq R_{ij}^{(5)} \end{cases}$$

$S^{(1)}$  and  $S^{(2)}$  are cubic spline functions.  $\epsilon_{ij}$  and  $\sigma_{ij}$  are the Lennard-Jones parameters. The values we used are: 51.2 and 2.28 for hydrogen; 8.6 and 2.81 for carbon. Using this model, the code stabilizes the hydrocarbon by changing positions of the atoms and minimising the energy of the system.

## 2.2 Bending angle of a relaxed heterojunction

Pristine carbon nanotubes face minimum bond-strain as it is fully made of hexagons, it is just a folded graphene sheet. As we introduce 5-7 defects, the bonds near these defects gets strained due to stretch or compression. The figure below demonstrates how each defect effects the bonds near a junction region.

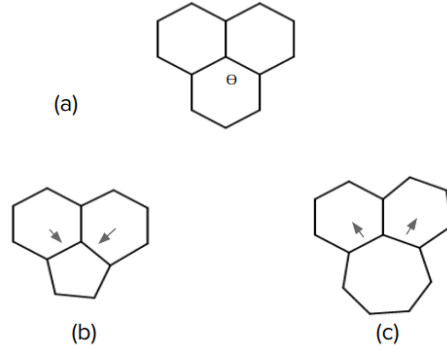


Figure 2.1: (a) Minimum strain in case of three hexagons (b) Pentagon defect stretches two hexagons (c) Heptagon defect compresses two hexagons

To recall, we used 5-7 defects create heterojunctions. We used two types of 5-7 defects, A-type and B-type, to join two carbon nanotubes at a junction (heterojunction).

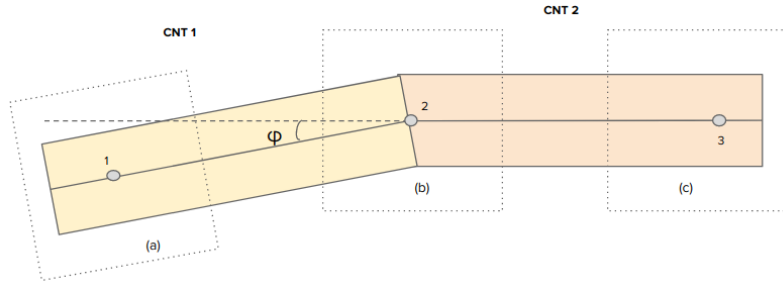


Figure 2.2: (a) and (c) regions are the edges of the CNTs, (b) region is the heterojunction; (1), (2) and (3) are center of masses of the regions (a), (b) and (c)

After relaxing a carbon nanotube heterojunction (CNT-HJ), it bends about the junction if it is more strained than usual. To calculate the degree of how much it bent, I calculated the center of masses for the regions (shown in figure above). The bending angle  $\phi$  is the angle made by the three of them at the junction.

The bending angle is governed by two factors:

- Number of defects
- Uniformity in the distribution of the defects around the junction

## 2.3 Results

Here are few examples on how number of defects and their uniformity changes the bending angle  $\phi$ . The top figures are interfaces at junction of the CNT HJs opened up (sheet form) and **the defects highlighted (white)**. The **bottom figures are CNT HJs (tube form)** after they are relaxed.

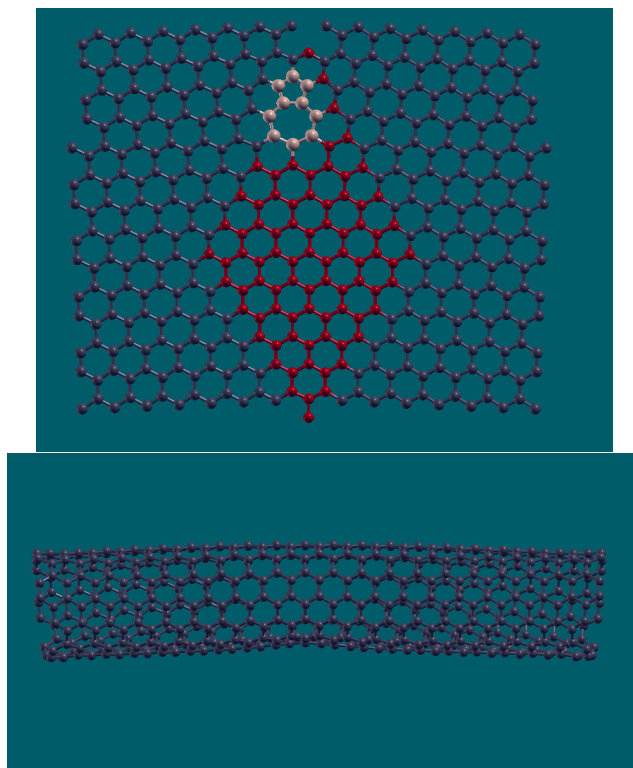


Figure 2.3: 1 A type defect(7,6-7,6);  $\phi = 8.146$  deg

In the above figure, we can see using a single defect strains the bonds near junction region resulting in bend structure after relaxation.

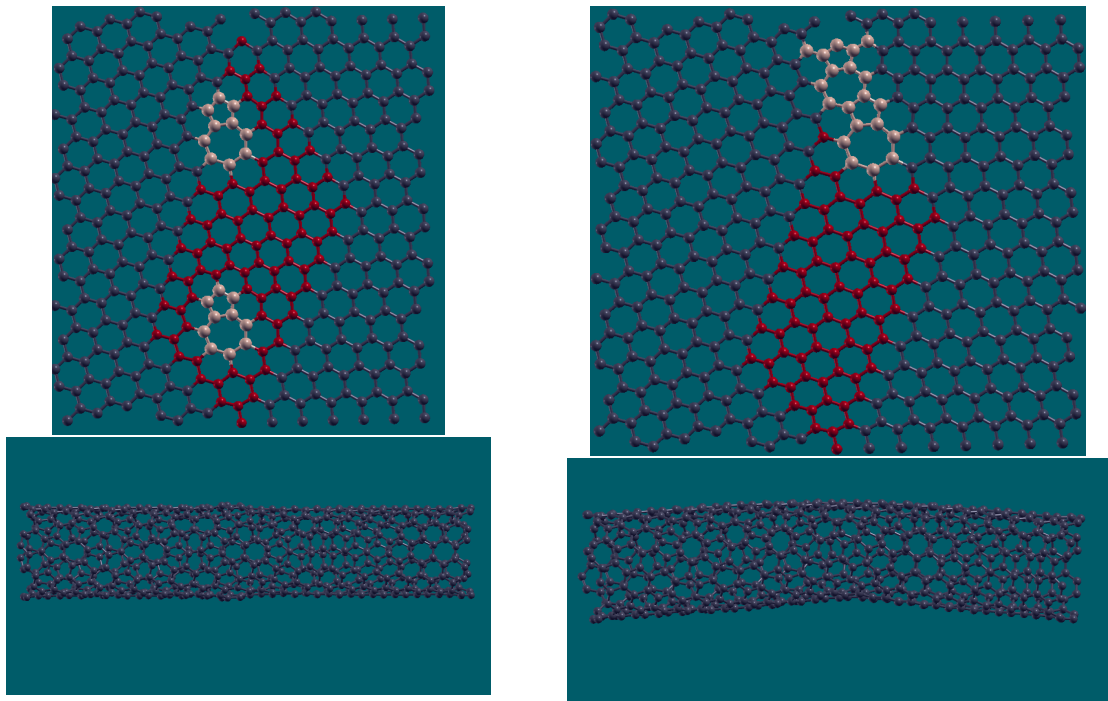


Figure 2.4: 2 A type defect(uniform)  
(10,4-6,8);  $\phi = \mathbf{0.01}$  deg

Figure 2.5: 2 A type defect(lumped)  
(10,4-6,8);  $\phi = \mathbf{13.017}$  deg

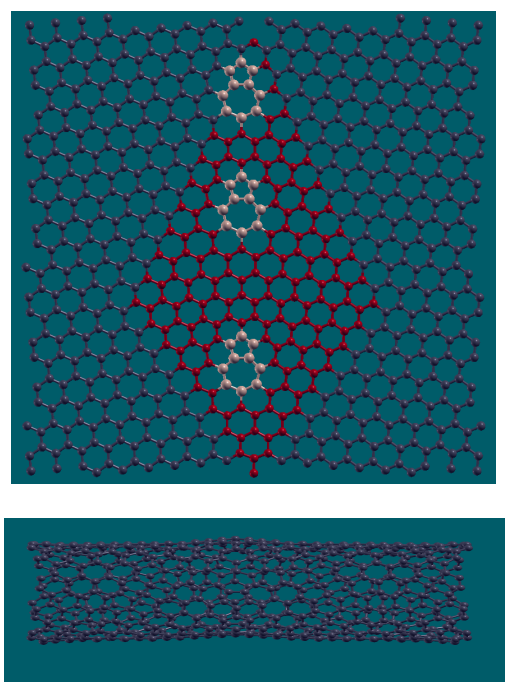
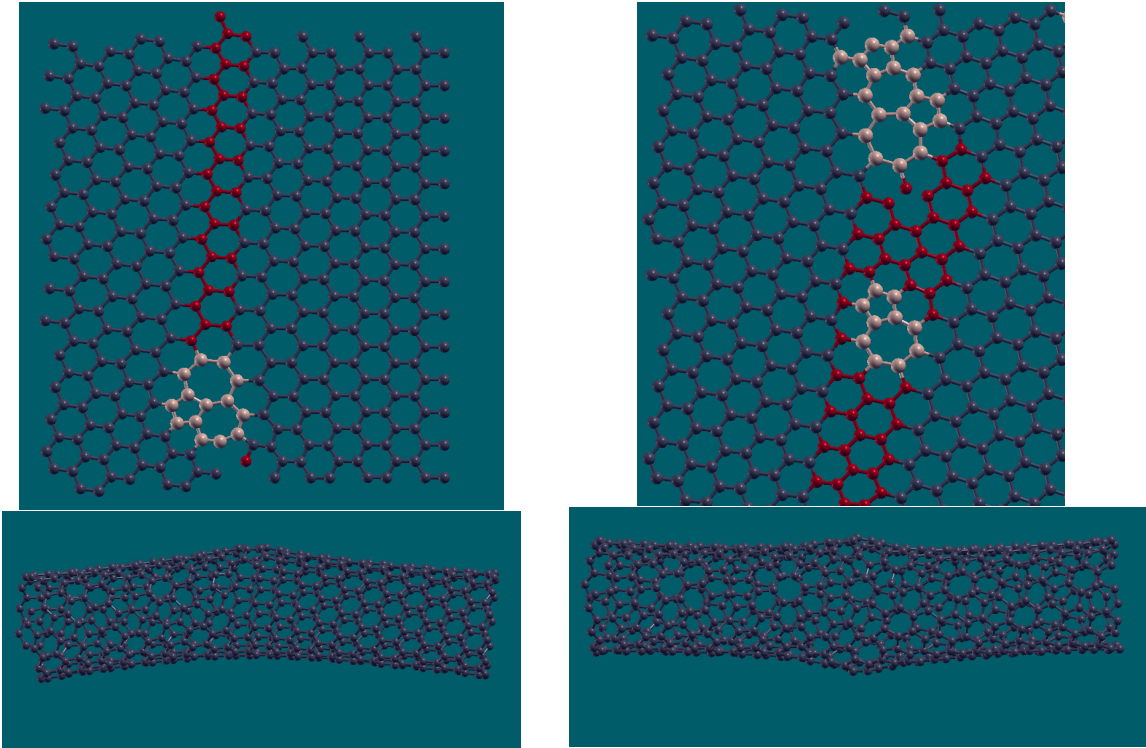


Figure 2.6: 3 A type defect(uniform) (11,8-11,8);  $\phi = \mathbf{2.07}$  deg



Defects	Bending angle ( $\phi$ )
1A type [7,6-7,6]	8.146
2A type (lumped) [10,4-6,8]	13.017
2A type (uniform) [10,4-6,8]	$\sim 0.01$
3A type (uniform) [11,8-11,8]	2.07
1B type [2,12-13,0]	9.83
1B + 1A type [12,2-5,10]	4.413
1B + 2A type [10,5-8,6]	3.117

In the figure (3.2), addition of another A-type defect to a existing A-type in equi-spaced position balances out the first defect, hence reducing  $\phi$  significantly (almost linear, though the defects bulks out at the junction). While in figure (3.3), addition of the same A-defect close to the first A-defect causes dis-balance which leads to bending of the tube. Other examples are given in the above table.

# Chapter 3

## Electronic structure theory

### 3.1 Tight Binding Model

Tight-binding model is the simplest approach for electronic structure of periodic solids. TB model considers an approximate set of wave functions constructed from the superposition of the wave functions for isolated atoms located at each atomic sites. The model provides a fairly accurate description of electronic structure near the Fermi energy level, which can be matched with experimental results by tuning the input parameters. Within the TB Hamiltonian wave function of wave function of a system of atoms is considered to be a linear combination of atomic orbitals  $\{\phi(r)\}$  ( $R=0$ ),

$$H_{at}\phi_j(r) = E_j\phi_j(r) \quad (3.1)$$

where the  $H_{at}$  is the atomic hamiltonian and  $E_j$  are the energy levels of a single atoms. Now for cell periodic Hamiltonian we know,

$$H(r) = H(r + R) \quad (3.2)$$

where  $\mathbf{R}=n_1a_1 + n_2a_2 + n_3a_3$  is real space vector and  $\{ni\} \rightarrow \mathbb{Z}$ . Bloch's theorem gives us,

$$\psi_{n\mathbf{k}}(\mathbf{r}) = u_{n\mathbf{k}}(\mathbf{r})e^{i\mathbf{k}\cdot\mathbf{r}} \quad (3.3)$$

where  $= u_{n\mathbf{k}}(\mathbf{r})$  has has the cell periodicity of the Hamiltonian,  $n$  is the band index and within Born-von Karman boundary condition the allowed values of  $k$ , also known

as crystal momentum are given by:

$$\mathbf{k} = \sum_{i=1}^3 \frac{m_i}{N_i} \mathbf{b}_i \quad (3.4)$$

where  $m_i$  is integer and  $\mathbf{b}_i$  are the reciprocal lattice vectors. The Bloch function  $\psi_{n\mathbf{k}}(\mathbf{r})$  can be expanded in the basis of Wannier functions  $\phi_n(\mathbf{r} - \mathbf{R})$  as

$$\psi_{n\mathbf{k}}(\mathbf{r}) = \sum_{\mathbf{R}} e^{i\mathbf{k}\cdot\mathbf{R}} \phi_n(\mathbf{r} - \mathbf{R}) \quad (3.5)$$

Hence we can write the Schrodinger equation for the crystal can be written as,

$$H\psi_{m\mathbf{k}}(\mathbf{r}) = (H_{at} + \Delta V) \psi_{m\mathbf{k}}(\mathbf{r}) = \varepsilon_m(\mathbf{k}) \psi_{m\mathbf{k}}(\mathbf{r}) \quad (3.6)$$

where,  $H$  is the crystal Hamiltonian and  $\Delta V$  contains the corrections to reproduce the full periodic potential of the crystal. Now multiplying Eq.3.5 by  $\phi_m^*(\mathbf{r})$  and using Eq.3.1,

$$(\varepsilon_m(\mathbf{k}) - E_m) \int \phi_m^*(\mathbf{r}) \psi_{m\mathbf{k}}(\mathbf{r}) d^3r = \int \phi_m^*(\mathbf{r}) \Delta V \psi_{m\mathbf{k}}(\mathbf{r}) d^3r \quad (3.7)$$

Now we will construct a representation of a given Hamiltonian, in the basis of a chosen set of  $N$  number of orthonormal localized functions  $\{\phi_i(\mathbf{r})\}$ . Wannier functions are considered as a linear combinations of the chosen basis functions as :

$$W_m(\mathbf{r}, \mathbf{R}) = \sum_n^N C_{mn} \phi_n(\mathbf{r} - \mathbf{R}). \quad (3.8)$$

Hence,

$$\psi_{m\mathbf{k}} = \sum_n \sum_R C_{mn} \phi_n(\mathbf{r} - \mathbf{R}) e^{ik.R} \quad (3.9)$$

Simplifying and imposing the orthonormality for the atomic wave function for

Bloch energy of the state,

$$\begin{aligned}
 (\varepsilon_m(\mathbf{k}) - E_m) \sum_n \sum_{\mathbf{R}} \int d^3r \phi_m^*(\mathbf{r}) \phi_n(\mathbf{r} - \mathbf{R}) e^{i\mathbf{k}\cdot\mathbf{R}} &= \sum_n \int d^3r \phi_m^*(\mathbf{r}) \Delta V \phi_n(\mathbf{r}) \\
 &\quad + \sum_n \sum_{\mathbf{R}} \int d^3r \phi_m^*(\mathbf{r}) \Delta V \phi_n(\mathbf{r} - \mathbf{R}) e^{i\mathbf{k}\cdot\mathbf{R}} \\
 (\varepsilon_m(\mathbf{k}) - E_m) \left( 1 + \sum_n \sum_{\mathbf{R}} \int d^3r \phi_m^*(\mathbf{r}) \phi_n(\mathbf{r} - \mathbf{R}) e^{i\mathbf{k}\cdot\mathbf{R}} \right) &= \int d^3r \phi_m^*(\mathbf{r}) \Delta V \phi_m(\mathbf{r}) \\
 &\quad + \sum_n \sum_{\mathbf{R}} \int d^3r \phi_m^*(\mathbf{r}) \Delta V \phi_n(\mathbf{r} - \mathbf{R}) e^{i\mathbf{k}\cdot\mathbf{R}}
 \end{aligned} \tag{3.10}$$

Therefore, the energy in terms of TB-matrix elements  $\beta_m$ ,  $\alpha_{m,n}$  and  $\gamma_{m,n}$

$$\varepsilon_m(\mathbf{k}) = E_m - \frac{\beta_m + \sum_{\mathbf{R}} \sum_n \gamma_{m,n}(\mathbf{R}) e^{i\mathbf{k}\cdot\mathbf{R}}}{1 + \sum_{\mathbf{R}} \sum_n \alpha_{m,n}(\mathbf{R}) e^{i\mathbf{k}\cdot\mathbf{R}}}$$

where  $E_m$  is onsite energy of the m-th atomic orbital.

$$\begin{aligned}
 \beta_m &= - \int d^3r \Delta V |\phi_m(\mathbf{r})|^2 \\
 \alpha_{m,n}(\mathbf{R}) &= \int d^3r \phi_m^*(\mathbf{r}) \phi_n(\mathbf{r} - \mathbf{R}) \\
 \gamma_{m,n}(\mathbf{R}) &= - \int d^3r \phi_m^*(\mathbf{r}) \Delta V \phi_n(\mathbf{r} - \mathbf{R}).
 \end{aligned} \tag{3.11}$$

- $\beta_m$  represents the change in atomic energy due to the presence of periodic potential and this gives a small correction within TB-formalism.
- $\alpha_{m,n}$  is the overlap of atomic orbitals located at different sites which is negligible within TB approximation.
- $\gamma_{m,n}$  is the inter-atomic overlap integral between two atomic sites which is also known as 'hopping' parameter.

The hopping parameter will be different for nearest or next-nearest neighbor overlap and its sign will be positive or negative depending on the degree of overlap and orientation of the orbitals in neighboring sites.

Now in second quantization formalism, we vacuum state  $|\Omega\rangle$  and field operators  $a_\lambda, a_\lambda^\dagger$  the  $N$  particle many-body state can be written as,

$$\frac{1}{\sqrt{\prod_\lambda n_\lambda!}} a_{\lambda_N}^\dagger \dots a_{\lambda_1}^\dagger |\Omega\rangle = |\lambda_1, \lambda_2, \dots, \lambda_N\rangle \quad (3.12)$$

where the field operators satisfies the following anti-commutation relations, shown below:

$$\{a_\lambda, a_\mu^\dagger\} = \delta_{\lambda\mu}, \quad \{a_\lambda, a_\mu\} = \{a_\lambda^\dagger, a_\mu^\dagger\} = 0.$$

Single particle or one-body operators  $\hat{O}_1$  acting on a  $N$  particle Hilbert space (Eq. 3.12) in general can be written as

$$\hat{O}_1 = \sum_{m=1}^N \hat{o}_m$$

where,  $\hat{o}_m$  is a single particle operator acting on  $m$ -th particle. The same in terms of field operators in any general basis can be written as

$$\hat{O}_1 = \sum_{\mu\nu} \langle \mu | \hat{o}_1 | \nu \rangle a_\mu^\dagger a_\nu$$

Two body operator  $(\hat{O}_2)$  which represent the pairwise interaction between two particles are taken can be written as

$$\hat{O}_2 = \sum_{\mu\mu'\nu\nu'} \langle \mu\mu' | \hat{o}_2 | \nu\nu' \rangle a_{\mu'}^\dagger a_\mu^\dagger a_\nu a_{\nu'}$$

Now we first take a generic interacting Hamiltonian for  $N$  particle systems,

$$H = H_0 + V_{e-e} = \sum_{i=1}^N \left( \frac{p_i^2}{2m_e} + V_{ext}(\mathbf{r}_i) \right) + \frac{1}{2} \sum_{i \neq j}^N V_{ee}(\mathbf{r}_i - \mathbf{r}_j)$$

We can express this equation in terms of field operators  $c_{i\sigma}$  and  $c_{i\sigma}^\dagger$  which can be defined on the basis of localized orbitals  $\phi_i(\mathbf{r})$  as

$$|\phi_i\rangle = \int_0^V d\mathbf{r} |r_\sigma\rangle \langle r_\sigma | \phi_{i\sigma}\rangle$$

where  $|\phi_i\rangle = c_{i\sigma}^\dagger |\Omega\rangle$  and  $|r_\sigma = c_\sigma^\dagger(\mathbf{r})| \Omega\rangle$  leads to

$$c_{i\sigma}^\dagger = \int_0^V d\mathbf{r} c_\sigma^\dagger(\mathbf{r}) \phi_i^*(\mathbf{r})$$

where,  $c_{i\sigma}^\dagger$  can be called as a creation operator which creates an electron at site  $i$  with spin  $\sigma$  and they obey fermionic commutation relations. Thus, w.r.t to these operators, the one body operator becomes the following form,

$$\hat{h}_1 = \sum_{i\sigma} \epsilon_i c_{i\sigma}^\dagger c_{i\sigma} + \sum_{i\neq j} \sum_{\sigma} t_{ij} c_{i\sigma}^\dagger c_{j\sigma} \quad (3.13)$$

where,  $\epsilon_i = \langle i | H_0 | i \rangle$  represents onsite term and  $t_{ij} = \langle i | H_0 | j \rangle$  represents the hopping term respectively.  $t_{ij} < 0$  for bound states. This  $\hat{h}_1$  describes non-interacting Hamiltonian in second quantized notation.

Now we take a minor detour to derive a second quantized description of an electron in a periodic potential. Recalling the TB Hamiltonian in presence of a periodic potential  $V(\mathbf{r}) = \sum_{\mathbf{K}} V_{\mathbf{K}} e^{i\mathbf{K}\cdot\mathbf{r}}$  and using  $c_i = \frac{1}{\sqrt{N}} \sum_{\mathbf{k}} c_{\mathbf{k}} e^{i\mathbf{k}\cdot\mathbf{R}_i}$  which annihilate an electron at lattice site  $\mathbf{R}_i$ . Hence, in Fourier space  $H = H_0 + V(\mathbf{r})$  leads to

$$H = \sum_{\mathbf{k}} \epsilon(\mathbf{k}) c_{\mathbf{k}}^\dagger c_{\mathbf{k}} + \sum_{\mathbf{k}, \mathbf{K}} V_{\mathbf{K}} c_{\mathbf{k}+\mathbf{K}}^\dagger c_{\mathbf{k}}$$

where,  $c_{\mathbf{k}}^\dagger$  ( $c_{\mathbf{k}}$ ) is creation(annihilation) operator and  $\epsilon(\mathbf{k})$  provides the dispersion relation. As a further example the Hamiltonian for two sites (c, d) per unit cell using (Eq. 3.13) can be written as,

$$H = t \sum_i \left( c_i^\dagger d_i + d_i^\dagger c_{i+1} + \text{h.c.} \right) + \sum_i \varepsilon_c c_i^\dagger c_i + \sum_i \varepsilon_d d_i^\dagger d_i$$

Position of the two sites in j-th unit cell can be define as,  $r = a.j + r_c$  for c-site and for d-site  $r = a.j + r_d$  where a is unit cell parameter. Now, considering discrete Fourier transform of this operators and simplifying we can write,

$$\sum_i c_i^\dagger d_i = \sum_k c_k^\dagger d_k e^{ik(r_d - r_c)}, \quad \sum_i d_i^\dagger c_{i+1} = \sum_k d_k^\dagger c_k e^{ik(r_c - r_d)}$$

Hence the final Hamiltonian,

$$H = t \sum_k \left( c_k^\dagger d_k e^{ik(r_d - r_c)} + d_k^\dagger c_k e^{ik(r_c - r_d)} + \text{h.c.} \right) + \sum_k \varepsilon_c c_k^\dagger c_k + \sum_k \varepsilon_d d_k^\dagger d_k$$

which implies,

$$H = \sum_k \begin{pmatrix} c_k^\dagger & d_k^\dagger \end{pmatrix} \begin{pmatrix} \varepsilon_c & 2t \cos(kr_{cd}) \\ 2t \cos(kr_{cd}) & \varepsilon_d \end{pmatrix} \begin{pmatrix} c_k \\ d_k \end{pmatrix}$$

$$H = \sum_k \begin{pmatrix} c_k^\dagger & d_k^\dagger \end{pmatrix} H_k \begin{pmatrix} c_k \\ d_k \end{pmatrix}$$

Hence for N-sites per unit cell, the  $H_k$  will be  $N \times N$  matrix and diagonalization of which gives eigenvalues and eigenfunctions.

Returning to our previous discussion of interacting electrons in second quantized notation. Two body interaction term can be written as,

$$\hat{h}_2 = \sum_{ijkl} \sum_{\sigma, \sigma'} V_{ijkl} c_{i\sigma}^\dagger c_{j\sigma'}^\dagger c_{k\sigma'} c_{l\sigma} \tag{3.14}$$

where the interaction parameter,

$$V_{ijkl} = \frac{1}{2} \iint d\mathbf{r} d\mathbf{r}' \phi_i^\dagger(\mathbf{r}) \phi_j^\dagger(\mathbf{r}') \frac{e^2}{|\mathbf{r} - \mathbf{r}'|} \phi_k(\mathbf{r}') \phi_l(\mathbf{r})$$

Thus the generalized Hamiltonian combining eq. 3.13 and eq. 3.14 in second quantization we get,

$$H = \sum_{i,\sigma} \epsilon_i c_{i\sigma}^\dagger c_{i\sigma} - \sum_{i,j} \sum_{\sigma} t_{ij} c_{i\sigma}^\dagger c_{j\sigma} + \sum_{ijkl} \sum_{\sigma\sigma'} V_{ijkl} c_{i\sigma}^\dagger c_{j\sigma'}^\dagger c_{k\sigma'} c_{l\sigma}. \quad (3.15)$$

The interaction term  $V_{ijkl}$  has two important contributions which can be written in terms of its indices i, j, k and l as :

- For  $i = l$  and  $j = k$ ,  $V_{ijkl} = V_{ijji} \equiv V_{ij}$  is known as direct term which couples with the density operator  $\hat{n}_i = \sum_{\sigma} c_{i\sigma}^\dagger c_{i\sigma}$  at different site as,

$$\sum_{i,j} V_{ij} \hat{n}_i \hat{n}_j$$

- For  $i = k$  and  $j = l$ ,  $V_{ijkl} = V_{ijij} \equiv J_{ij}$  is known as exchange term. Using the completeness relation  $\sigma_{\alpha\beta} \cdot \sigma_{\gamma\delta} = 2\delta_{\alpha\delta}\delta_{\beta\gamma} - \delta_{\alpha\beta}\delta_{\gamma\delta}$

$$\sum_{i,j} \sum_{\sigma,\sigma'} V_{ijij} c_{i\sigma}^\dagger c_{j\sigma'}^\dagger c_{i\sigma'} c_{j\sigma} = -2 \sum_{i,j} J_{ij} \left( \hat{\mathbf{S}}_i \hat{\mathbf{S}}_j + \frac{1}{4} \hat{n}_i \hat{n}_j \right)$$

where  $\hat{\mathbf{S}}$  is spin operator.

## 3.2 Hubbard Model

In the atomic limit, the most important interaction considered is the Coulomb interaction term which is maximum between the two electrons residing on the same site. The electrostatic energy of two intra-site electrons which is also known as onsite Coulomb interaction from eq. 3.14 can be written as

$$\sum_i \sum_{\sigma,\sigma'} V_{iiii} c_{i\sigma}^\dagger c_{i\sigma'}^\dagger c_{i\sigma'} c_{i\sigma} = U \sum_i \hat{n}_{i\uparrow} \hat{n}_{i\downarrow}$$

Hence from eq. 3.15

$$H = H_t + H_{int} = \sum_{i,\sigma} \epsilon_i c_{i\sigma}^\dagger c_{i\sigma} - \sum_{i,j} \sum_{\sigma} t_{ij} c_{i\sigma}^\dagger c_{j\sigma} + U \sum_i n_{i\uparrow} n_{i\downarrow}. \quad (3.16)$$

John Hubbard first introduced this simple interacting Hamiltonian with the inclusion of onsite Coulomb interaction which obeyed Pauli's exclusion principle, in 1963 which came to known as Hubbard model[10] where  $U$  is known as Hubbard  $U$  term. In general, the inter-site Coulomb interaction is considered to be screened and have a negligible impact however since Coulomb interaction is long range so a proper estimation of  $U$  for different system is an important aspect of this model. Depending on the degree of localization of the orbitals in some scenarios it is necessary to include nearest, next nearest Coulomb interactions leading to extended Hubbard model.

### 3.3 Mean Field approximation

This is a simple approximation done to reduce the complexity of many body Hamiltonian in which all many body interactions are replaced by an effective or mean-field of interactions acting on a single body. According to mean-field approximation, all particle operator can be shown in terms of number fluctuations ( $\delta n_i$ ) around the mean value ( $\langle n_i \rangle$ ). Hence,

$$n_{i\sigma} = \langle n_{i\sigma} \rangle + \delta n_{i\sigma}, \sigma = \uparrow, \downarrow.$$

and the two body interaction term becomes,

$$\begin{aligned} Un_{i\uparrow} n_{i\downarrow} &= U (\langle n_{i\uparrow} \rangle + \delta n_{i\uparrow}) (\langle n_{i\downarrow} \rangle + \delta n_{i\downarrow}) \\ &= U (\langle n_{i\uparrow} \rangle \langle n_{i\downarrow} \rangle + \langle n_{i\uparrow} \rangle \delta n_{i\downarrow} + \langle n_{i\downarrow} \rangle \delta n_{i\uparrow} + \delta n_{i\uparrow} \delta n_{i\downarrow}) \end{aligned}$$

Now, within mean-field approximation (neglecting the correlation of fluctuations ( $\delta n_{i\uparrow} \delta n_{i\downarrow}$ )) and using  $\delta n_{i\sigma} = n_{i\sigma} - \langle n_{i\sigma} \rangle$

$$U \sum_i n_{i\uparrow} n_{i\downarrow} = U \sum_i (n_{i\uparrow} \langle n_{i\downarrow} \rangle + n_{i\downarrow} \langle n_{i\uparrow} \rangle - \langle n_{i\uparrow} \rangle \langle n_{i\downarrow} \rangle)$$

After a direct Hartree-Fock decoupling of the interaction term, the mean-field Hubbard Hamiltonian(MFH) can be written as a sum of Hamiltonian for spins(up & down) and a constant term as :

$$\begin{aligned} H_{MF} &= H_{\uparrow} + H_{\downarrow} + C \\ H_{\uparrow} &= -t \sum_{\langle i,j \rangle} c_{i\uparrow}^{\dagger} c_{j\uparrow} + U \sum_i n_{i\uparrow} \langle n_{i\downarrow} \rangle \\ H_{\downarrow} &= -t \sum_{\langle i,j \rangle} c_{i\downarrow}^{\dagger} c_{j\downarrow} + U \sum_i \langle n_{i\uparrow} \rangle n_{i\downarrow} \\ C &= -U \sum_i \langle n_{i\uparrow} \rangle \langle n_{i\downarrow} \rangle. \end{aligned}$$

Thus the Hubbard Hamiltonian eq. 3.16 reduces to two matrices of size  $N \times N$  with  $2N$  mean-field parameters for up and down densities and the above equation suggests a self-consistent solution, which is a characteristic of a mean-field approach. Within this approximation, the Hubbard model Hamiltonian transform into two Hamiltonian for two opposite spins(up-  $\uparrow$ ,down-  $\downarrow$ ) where mean-field term for one of the spin ( $\uparrow$ ) depends on the average occupation of the opposite spin ( $\downarrow$ ,  $\langle n_{i\downarrow} \rangle$ ). So to calculate the ground state energy and density, this Hamiltonian need to be solved in a self-consistent way. Starting from an initial guess density of electrons of spin  $\sigma$  ( $\langle n_{i\sigma} \rangle$ ), the following steps are repeated until the convergence criterion set in terms of total energy or density is satisfied.

Fermi energy ( $\varepsilon_{F\sigma}$ ) is obtained as,

$$\int_{-\infty}^{\infty} D(\varepsilon_{\sigma}) f(\varepsilon_{\sigma} - \varepsilon_{F\sigma}) d\varepsilon_{\sigma} = N_{e\sigma}$$

where,  $D(\varepsilon)$  is density of states and  $f(\varepsilon - \varepsilon_F)$  is Fermi function with Fermi energy  $\varepsilon_F$  at  $T = 0$ . Average number of particle at each site  $i (= j)$  for spin  $\sigma$  is

$$\langle n_{i\sigma} \rangle = \frac{1}{N} \sum_{\mathbf{k},j} |c_{i,\sigma}^j(\mathbf{k})|^2 f_{\mathbf{k}j\sigma} (\varepsilon_{\mathbf{k}j\sigma} - \varepsilon_{F\sigma}),$$

where  $c_{i,\sigma}^j(\mathbf{k})$  is weight of the  $j$ -th eigen state on  $i$ -th site for wave vector  $\mathbf{k}$ . For nonmagnetic ground state we set  $\langle n_\sigma \rangle = \langle n'_\sigma \rangle$ , whereas for anti-ferromagnetic ground state we set  $\varepsilon_{F\sigma} = \varepsilon'_{F\sigma}$ . For ferromagnetic ground state we calculate  $\varepsilon_{F\sigma}$  and  $\varepsilon'_{F'_\sigma}$  such that  $N_{e\sigma} - N_{e\sigma'}$  is equivalent to net magnetic moment.

## 3.4 Results

### 3.4.1 Magnetic CNT HJs

Prisitine carbon nanotubes do not show overall magnetism (Difference between up spin and down spin charge density). In zig-zag type CNTs(n,0), due to local sublattice symmetry we find absolute magnetism, i.e upspins and downspins occupying alternative sites. As we go towards arm-chair type (n,n), the local sublattice symmetry breaks and we lose spin charge density.

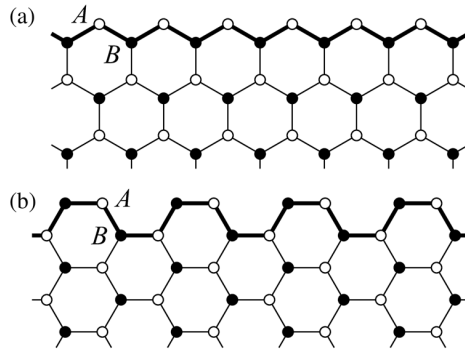


Figure 3.1: Edges showed by bold line: (a) Zig-zag type edges, (b) Armchair type edges

We took chiralities varying from (10,0) to (10,10). The visualisation of spin charge densities is given below.

Chiralities	Magnetism (BM/cell)
10, 0	Total spin = 0.0 Abs spin = 7.781
10, 3	Total spin = 0.0 Abs spin = 5.107
10, 6	Total spin = 0.0 Abs spin = 2.885
10, 10	Total spin = 0.0 Abs spin = 0

Table 3.1: Total and absolute magnetism by varying chiralities

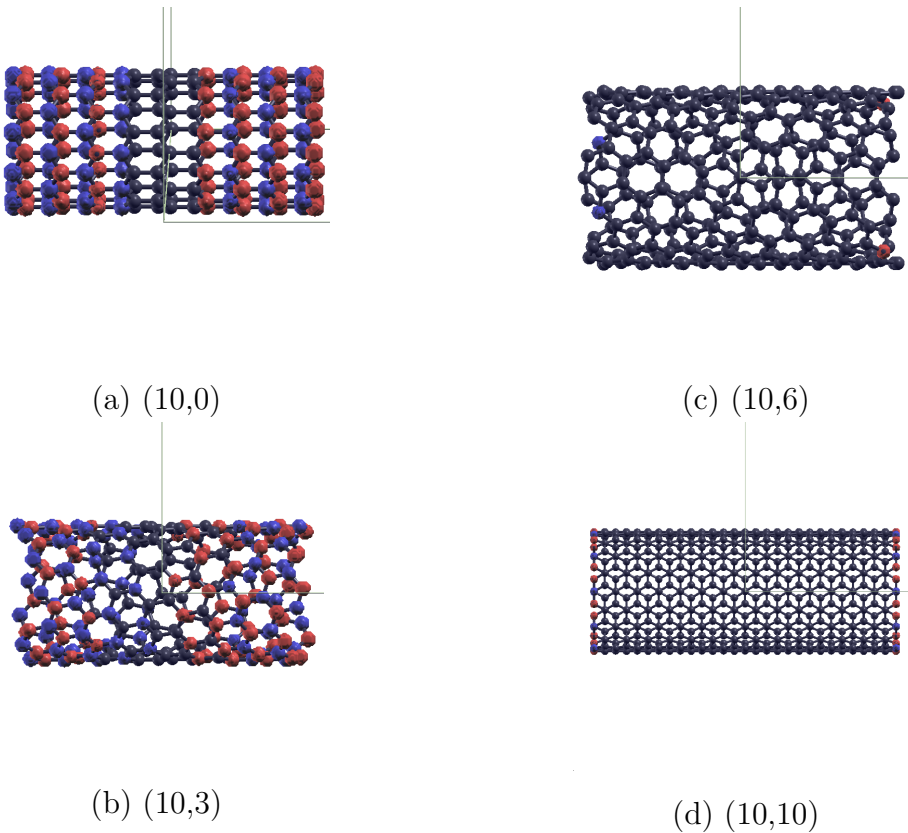


Figure 3.2: Visualisation of spin charge densities

The emergent net magnetic moment of the CNT HJs is routed at the interplay of the magnetic moments of individual CNTs and the degree of hindrance caused by the topological defects to the bipartite natures of the two CNTs. The topological

defects are therefore deterrence to inter-sublattice spin separation which otherwise causes anti ferromagnetic correlation between the two zigzag edges of the CNT HJs. Increase in number of topological defects would thus generally oppose localization of spins driven by Coulomb correlation. It is therefore possible that with a small number of defects at the interface a nearest neighbor ferromagnetic correlation nucleating at the topological defect can lead ferromagnetic order between the magnetic moments localized at the edges of the CNT segments at the two sides of the HJ. If we fix the number of defects then there should be a critical radius where such emergence of ferromagnetism should happen, as we see for (9,0)-(8,1), (10,0)-(9,1) , (11,0)-(10,1) and (12,0)-(11,1). Since the open edge of the (n,0) CNT hosts the maximum magnetic moment, which systematically decreases with increasing j for CNTs with chiralities (n-j,j), such a possibility should be possible in case of HJs made of CNTs (n-j1,j1) and (n-j2,j2) where j1 and j2 are much less than n.

### (9,0)-(n,m) series

Heterojunctions	Defects	Net mag.(BM/cell)	Absolute mag.(BM/cell)
(9,0)-(1,8)	1 A	4	5.473
(9,0)-(2,7)	2 A	0	5.415
(9,0)-(4,6)	2 A , 1 B	1	4.188
(9,0)-(5,5)	3 A , 1 B	1	6.267

### (10,0)-(n,m) series

Heterojunctions	Defects	Net mag.(BM/cell)	Absolute mag.(BM/cell)
(10,0)-(1,9)	1 A	6	7.825
(10,0)-(2,8)	2 A	2	5.425
(10,0)-(4,7)	2 A , 1 B	3	3.919
(10,0)-(6,6)	2 A , 2 B	2	5.012

## (11,0)-(n,m) series

Heterojunctions	Defects	Net mag.(BM/cell)	Absolute mag.(BM/cell)
(11,0)-(1,10)	1 A	2	7.766
(11,0)-(2,9)	2 A	4	6.267
(11,0)-(4,8)	2 A , 1 B	5	6.528
(11,0)-(6,6)	4 A , 1 B	3	4.387

## (12,0)-(n,m) series

Heterojunctions	Defects	Net mag.(BM/cell)	Absolute mag.(BM/cell)
(12,0)-(1,11)	1 A	0	8.166
(12,0)-(2,10)	2 A	0	8.001
(12,0)-(3,10)	1 A , 1 B	3	5.770
(12,0)-(4,9)	2 A , 1 B	1	6.528
(12,0)-(7,7)	3 A , 2 B	2	5.255

We see that introducing a single defect (slight tweaking) gives rise to huge net magnetism as we see in (9,0)-(1,8) and (10,0)-(1,9). It is not enough for introducing ferromagnetism in (11,0)-(1,10) or (12,0)-(1,11). The net magnetism reaches a peak for certain defect and then, overall net magnetism decreases as tweak it further towards an zig-zag armchair configuration (n,0-m,m).

Now we take different combinations: Metal-semiconductor(MS), Semiconductor-semiconductor(SS), Metal-metal(MM) to see how magnetism changes in different types of heterojunctions.

HJ type	Combinations	No of defects	Defect type
MS	(10,4-6,8)	2	2 A
	(6,9-12,2)	4	2 A , 1 B
	(13,0-6,9)	6	2 A , 2 B
SS	(2,12-13,0)	2	1 B
	(12,2-5,10)	3	1 A , 1 B
	(10,5-8,6)	4	2 A , 1 B
MM	(6,9-10,4)	2	1 B

For each of the combinations we took three lengths - 15 Å, 25 Å, 35 Å on both side. The magnetisation calculations are done in BM/cell.

**Length: 15 Å**

*MS heterojunctions:*

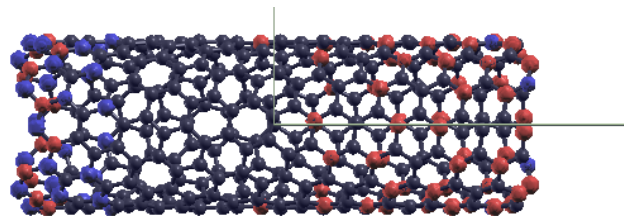


Figure 3.3: (10,4-6,8) HJ

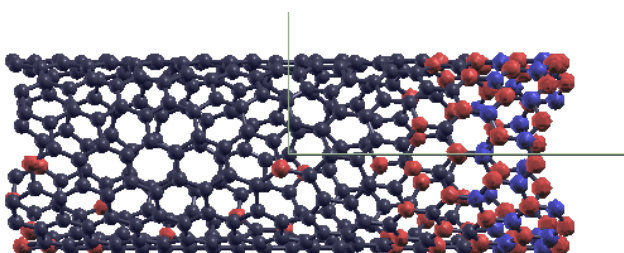


Figure 3.4: (6,9-12,2) HJ

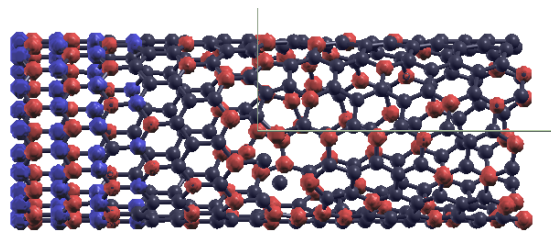


Figure 3.5: (13,0-6,9) HJ

*SS heterojunctions:*

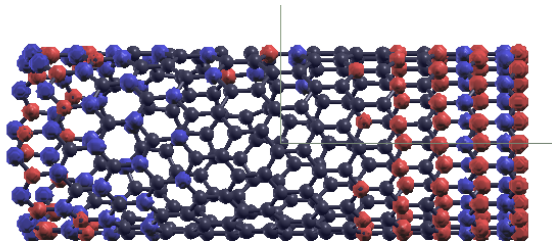


Figure 3.6: (2,12-13,0) HJ

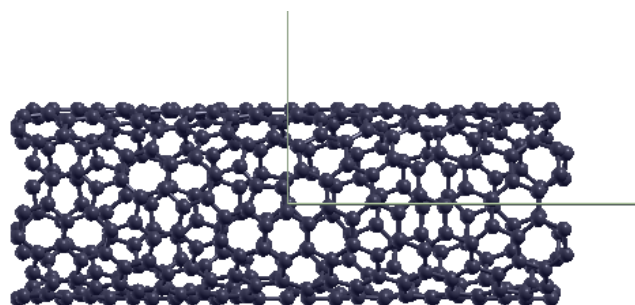


Figure 3.7: (10,5-8,6) HJ

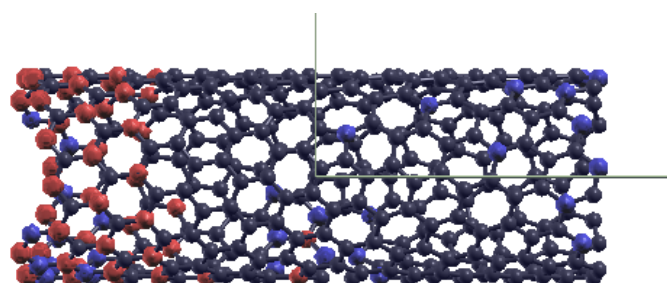


Figure 3.8: (12,2-5,10) HJ

*MM heterojunctions:*

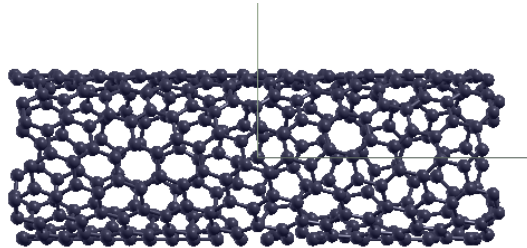


Figure 3.9: (6,9-10,4) HJ

Length: 15 Ang.	Metal-SC	SC-SC	Metal-Metal
2 defects	(10,4-6,8) Total mag= 0.0 Abs mag= 2.560	(2,12-13,0) Total mag= 1.0 Abs mag= 8.912	(6,9-10,4) Total mag= 0.0 Abs mag= 0.0
3 defects		(12,2-5,10) Total mag= 2 Abs mag= 3.264	
4 defects	(6,9-12,2) Total mag= 3 Abs mag= 3.944	(10,5-8,6) Total mag= 0.0 Abs mag= 0.0	
6 defects	(13,0-6,9) Total mag= 2 Abs mag= 5.411		

Table 3.2: Total and absolute magnetism for 15 Å length

As we take heterojunction combinations, please note that due to the topological defects (5-7 defects), the bipartite nature of CNTs is broken. Now, we check if some of those heterojunction structures can sustain magnetism.

**Length: 25 Å**

<b>Length: 25 Ang.</b>	Metal-SC	SC-SC	Metal-Metal
2 defects	(10,4-6,8) Total mag= 0.0 Abs mag= 0.0	(2,12-13,0) Total mag= 1.0 Abs mag= 9.32	(6,9-10,4) Total mag= 1 Abs mag= 1.334
3 defects		(12,2-5,10) Total mag= 3 Abs mag= 4.482	
4 defects	(6,9-12,2) Total mag= 3 Abs mag= 4.04	(10,5-8,6) Total mag= 0.0 Abs mag= 0.0	
6 defects	(13,0-6,9) Total mag= 4 Abs mag= 5.245		

Table 3.3: Total and absolute magnetism for 25 Å length

**Length: 35 Å**

<b>Length: 35 Ang.</b>	Metal-SC	SC-SC	Metal-Metal
2 defects	(10,4-6,8) Total mag= 0.0 Abs mag= 2.986	(2,12-13,0) Total mag= 1.0 Abs mag= 9.318	(6,9-10,4) Total mag= 1 Abs mag= 1.384
3 defects		(12,2-5,10) Total mag= 1.0 Abs mag= 6.475	
4 defects	(6,9-12,2) Total mag= 3 Abs mag= 3.975	(10,5-8,6) Total mag= 1.0 Abs mag= 3.654	
6 defects	(13,0-6,9) Total mag= 4 Abs mag= 5.261		

Table 3.4: Total and absolute magnetism for 35 Å length

We see from the above table that in 15 Å length category, (6,9-12,2) , (12,2-5,10) and (13,0-6,9) show some net magnetism.

Not only that, there are few spins around the defect regions.

We see from the above table that in 25 Å length category, (6,9-12,2) , (12,2-5,10)

and (13,0-6,9) again show net magnetism. Net magnetism in SS (12,2-5,10) and MM (6,9-10,4) increased compared to the 15 Å. This suggests that there might be some length dependency for the above cases.

We see from the above table that in 35 Å length category, (6,9-12,2) , (12,2-5,10) and (13,0-6,9) again show net magnetism. Now, net magnetism in SS (12,2-5,10) decreased and MS (13,0-6,9) increased in 25 and 35 Å with comparison to the 15 Å. SS (10,5-8,6) shows net magnetism in length 35 Å, which was not seen previously.

We see a general trend in MS combinations, that net magnetism increases with an increase in defects, in all lengths.

### 3.4.2 Projected DOS on tube axis

The **y-axis denotes the density of states (Projected DOS)** and **x-axis denotes the energy states (in eV)** taken at interval of 0.02 eV. The lengths taken are 15, 25 and 35 Ang as mentioned in the captions. The fermi energy is around 1 eV for each case.

To revise, the color codes for the PDOS of the regions are:

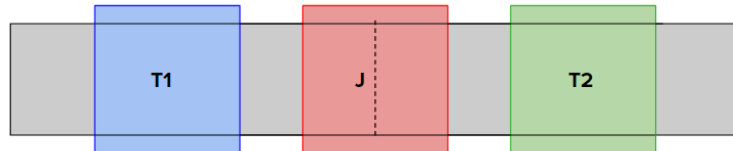


Figure 3.10: PDOS of (Blue) Tube 1; (Red) Junctions; (Green) Tube 2

**Metal-SC:**

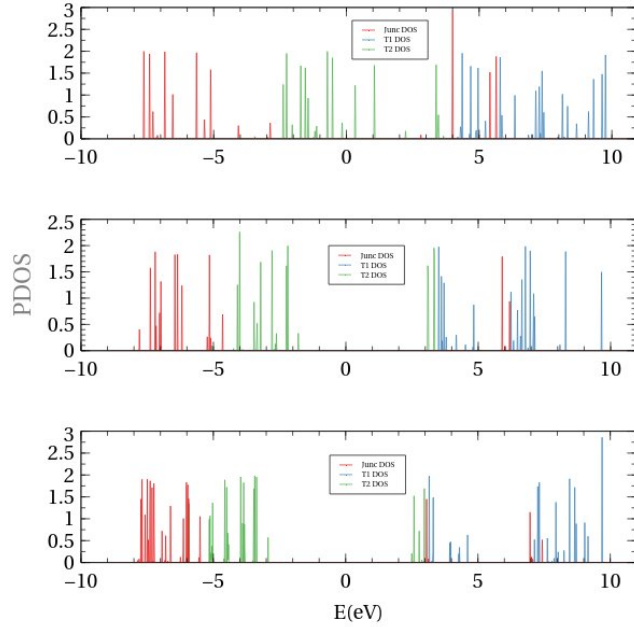


Figure 3.11: (10,4-6,8) HJ (a) Length: 15 Ang; (b) Length: 25 Ang; (c) Length: 35 Ang

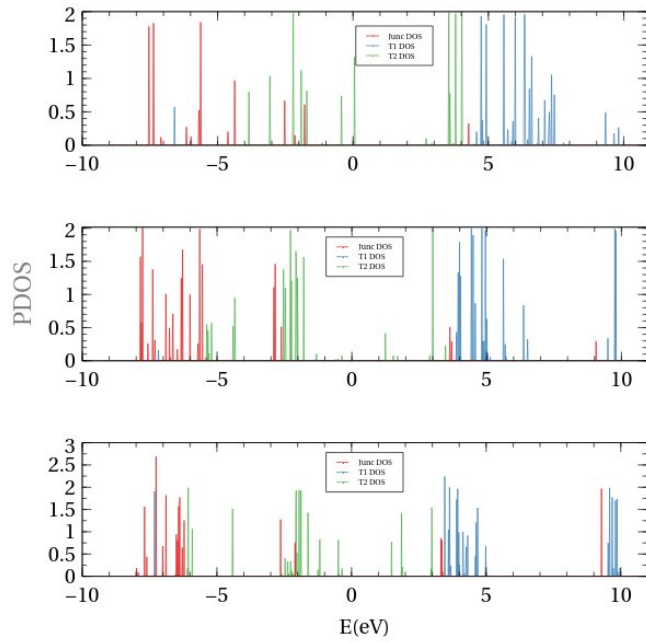


Figure 3.12: (6,9-12,2) HJ (a) Length: 15 Ang; (b) Length: 25 Ang; (c) Length: 35 Ang

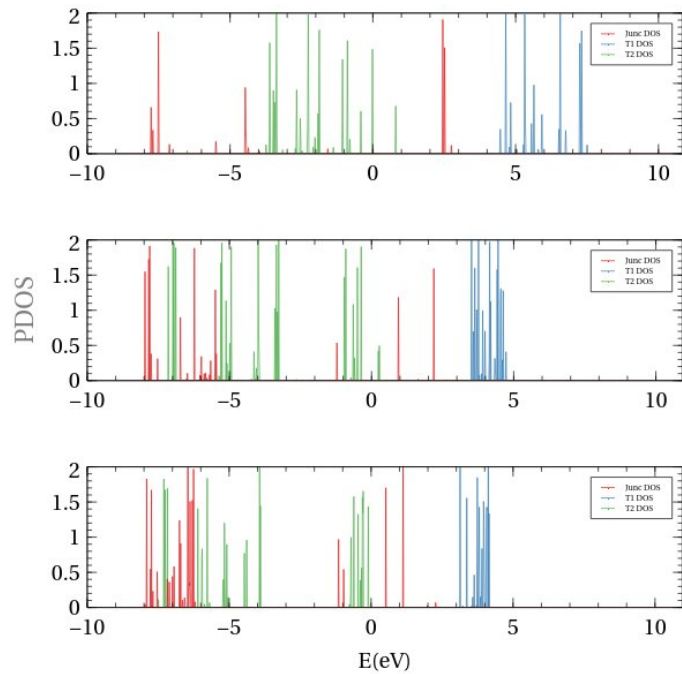


Figure 3.13: (13,0-6,9) HJ (a) Length: 15 Ang; (b) Length: 25 Ang; (c) Length: 35 Ang

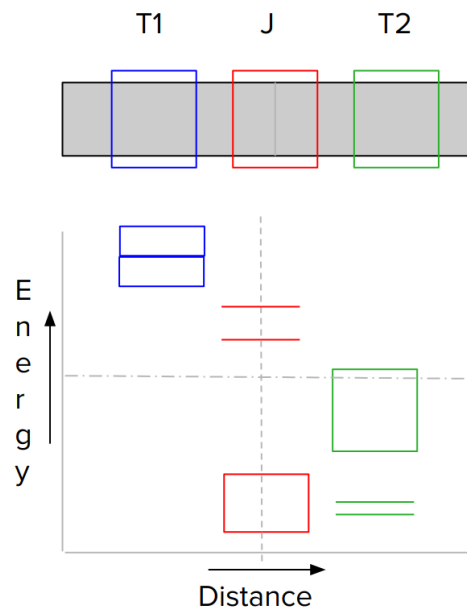


Figure 3.14: Energy diagram with respect to distance, for (13,0-6,9) HJ

**SC-SC:**

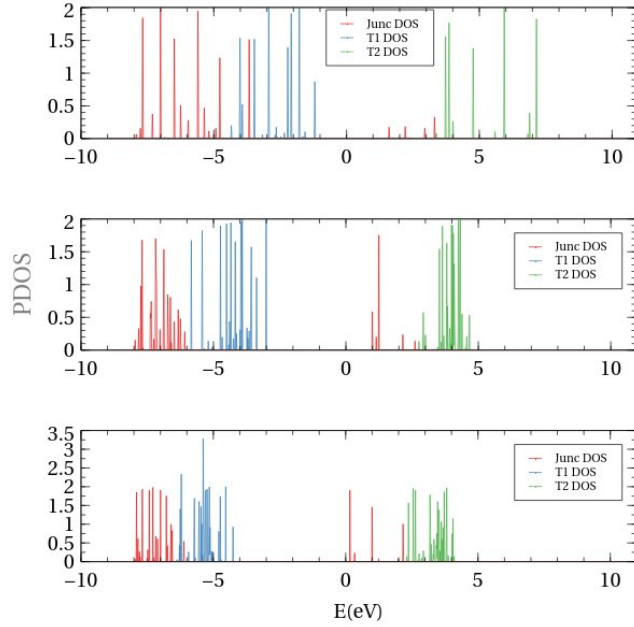


Figure 3.15: (2,12-13,0) HJ (a) Length: 15 Ang; (b) Length: 25 Ang; (c) Length: 35 Ang

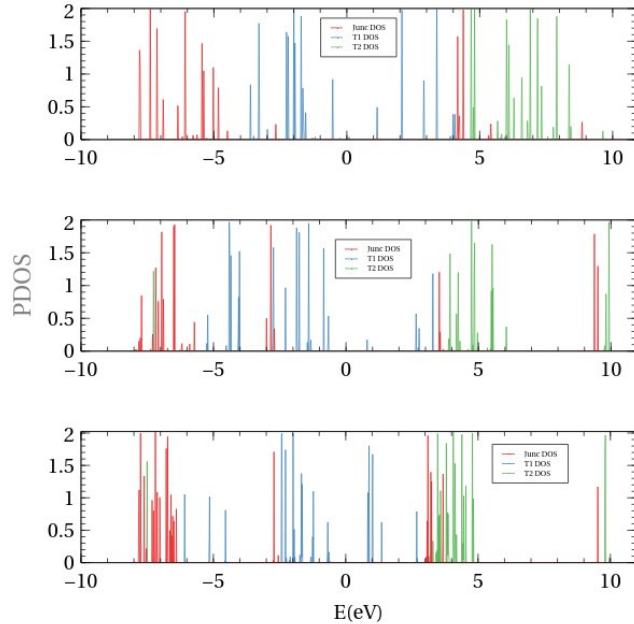


Figure 3.16: (12,2-5,10) HJ (a) Length: 15 Ang; (b) Length: 25 Ang; (c) Length: 35 Ang

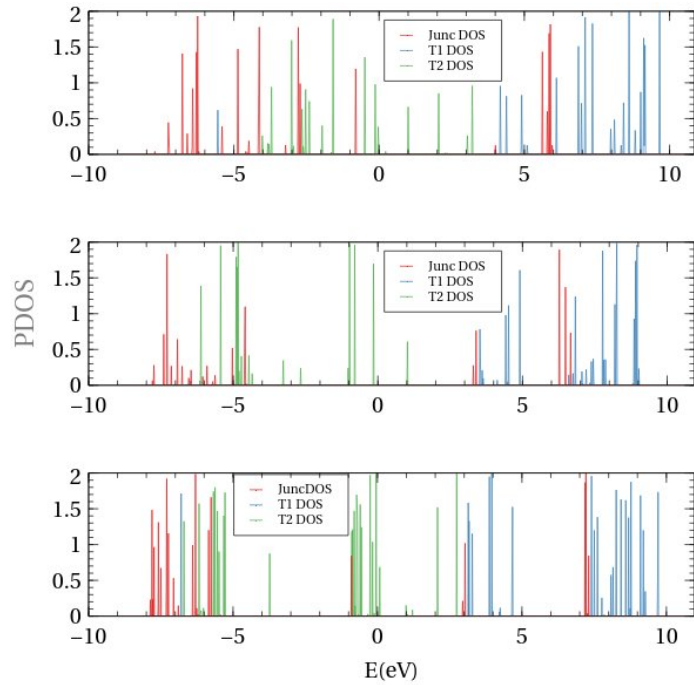


Figure 3.17: (10,5-8,6) HJ (a) Length: 15 Ang; (b) Length: 25 Ang; (c) Length: 35 Ang

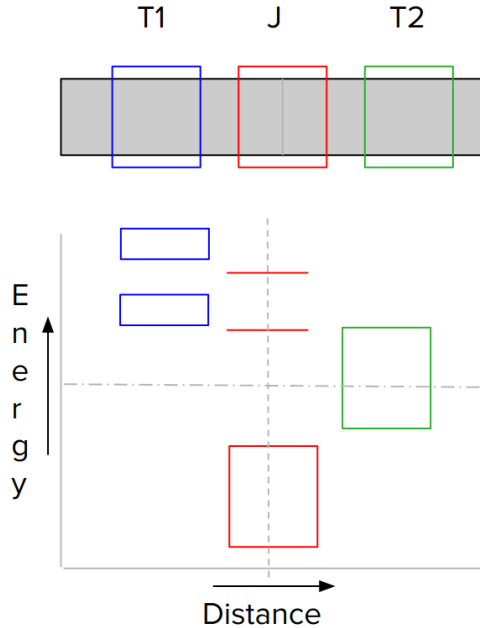


Figure 3.18: Energy diagram with respect to distance, for (10,5-8,6) HJ

# Chapter 4

## Electronic transport theory

### 4.1 Non-equilibrium Green's function formalism

Green's function is an important concept in transport calculation. We will see how it makes everything so elegantly simple.[1] However in this formalism, it is assumed that the **transport is coherent**, that is there are no phase breaking collisions.

#### 4.1.1 Contact-channel coupling

Let us begin with a simple scenario, a channel is coupled with one contact as shown below.

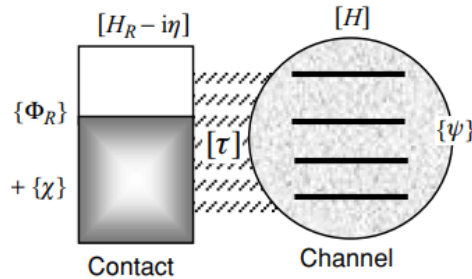


Figure 4.1: Channel coupled to a single contact[1]

We can write the Schrödinger equation (in matrix form) for the composite contact-channel system, with  $\Phi_R$  and  $\psi$  as the electron wavefunction in the contact and channel respectively,

$$\begin{pmatrix} EI_R - H_R + i\eta & -\tau^+ \\ -\tau & EI - H \end{pmatrix} \begin{Bmatrix} \Phi_R + \chi \\ \psi \end{Bmatrix} = \begin{Bmatrix} S_R \\ 0 \end{Bmatrix} \quad (4.1)$$

Here,

$H_R$  is the contact hamiltonian ( $R \times R$ ),  $H$  is the channel hamiltonian ( $d \times d$ ),  $\tau$  is the coupling matrix ( $d \times R$ ),  $\eta = 0^+ I_R$  is a positive infinitesimal times the identity matrix,  $i\eta\{\phi_R\}$  is the extraction of electron from the contact,  $S_R$  is the external source term ( $R \times 1$ ), which brings inhomogeneity in the Schrödinger equation.

The scattered waves  $\{\chi\}$  can be seen in this fashion, it arises from the "spilling over" of contact wavefunction  $\{\Phi_R\}$  in the isolated contact.

Equating in (4.1), we obtain,

$$\{\chi\} = G_R \tau^+ \{\psi\}$$

where,

$$G_R \equiv [EI_R - H_R + i\eta]^{-1} \quad (4.2)$$

$$\{\psi\} = [G]\{S\} \quad (4.3)$$

$$G \equiv [EI - H - \Sigma]^{-1} \quad (4.4)$$

$$\Sigma \equiv \tau G_R \tau^+ \quad (4.5)$$

$$\{S\} = \tau \{\Phi_R\} \quad (4.6)$$

$G$  and  $G_R$  are the green's functions for the channel and contact region respectively.  $\Sigma$  is called the self energy of the contact, which represents the modification to the contact due to coupling.

$\tau$  is the size of  $d \times R$  but in real space it couples with  $r$  threads (out of  $R$ ) of the reservoir or the contact. So the matrices can be truncated into,

$$\begin{matrix} \Sigma & \equiv & \tau & g_R & \tau^+ \\ (d \times) & & (d \times r) & (r \times r) & (r \times d) \end{matrix}$$

$$\begin{matrix} S & \equiv & \tau & \Phi_R \\ (d \times 1) & & (d \times r) & (r \times 1) \end{matrix}$$

$g_R$  is the surface green's function which is a subset ( $r \times r$ ) of the full green's function  $G_R$ , thus makes it much more easy to compute the inverse (Eq. 4.2) and thus other terms. There are computational methods developed to solve  $g_R$ , more on this in Section 4.1.2 .

Let's define the concept of spectral function  $A(E)$ .  $A(E)$  consists of local density of states as diagonal elements. Mathematically, in space,  $A(E)$  is defined as,

$$A(\vec{r}, \vec{r}'; E) = 2\pi \sum_{\alpha} \phi_{\alpha}(\vec{r}) \delta(E - \epsilon_{\alpha}) \phi_{\alpha}^*(\vec{r}')$$

It can be shown that,

$$A(E) = i [G - G^+] \quad (4.7)$$

where,  $G$  and  $G^+$  are retarded and advanced green's function.

Now we will just move to the next step, channel with two contacts - source and drain.

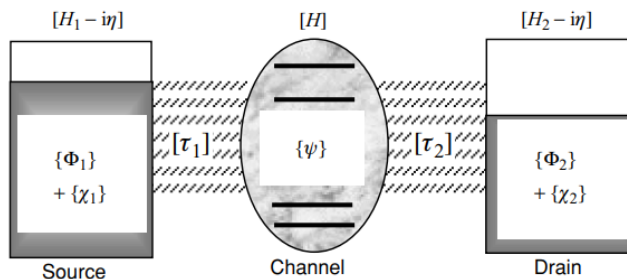


Figure 4.2: Channel coupled to source and drain[1]

The Schrödinger equation for the composite contact-1-device-contact-2 system can be written as (matrix form):

$$\begin{pmatrix} EI - H_1 + i\eta & -\tau_1^+ & 0 \\ -\tau_1 & EI - H & -\tau_2 \\ 0 & -\tau_2^+ & EI - H_2 + i\eta \end{pmatrix} \begin{Bmatrix} \Phi_1 + \chi_1 \\ \psi \\ \Phi_2 + \chi_2 \end{Bmatrix} = \begin{Bmatrix} S_1 \\ 0 \\ S_2 \end{Bmatrix}$$

The three columns and rows represents source channel and drain. Source-drain interactions are 0, hence 1st row 3rd element and 3rd row 1st element is zero. Source

and drain are coupled to channel by  $\tau_1$  and  $\tau_2$  respectively.  $H_1$  and  $H_2$  are source and drain Hamiltonian. Proceeding in similar way as before,

$$\{\chi_1\} = G_1 \tau_1^+ \{\psi\} \quad (4.8)$$

$$\{\chi_2\} = G_2 \tau_2^+ \{\psi\} \quad (4.9)$$

where,

$$G_1 = [EI - H_1 + i\eta]^{-1}$$

$$G_2 = [EI - H_2 + i\eta]^{-1}$$

are the Green's functions for source and drain (isolated reservoirs). Using Eq. (4.8 and 4.9) we eliminate  $\{\chi_1\}, \{\chi_2\}$  from the middle equation in the matrix form, we obtain

$$[EI - H - \Sigma_1 - \Sigma_2] \{\psi\} = \{S\} \quad (4.10)$$

where,  $\Sigma_1 = \tau_1 G_1 \tau_1^+$  and  $\Sigma_2 = \tau_2 G_2 \tau_2^+$  are the self-energy matrices. The corresponding broadening matrices are given by

$$\Gamma_1 = \tau_1 A_1 \tau_1^+ \quad \text{and} \quad \Gamma_2 = \tau_2 A_2 \tau_2^+$$

where,  $A_1 = i[G_1 - G_1^+]$  and  $A_2 = i[G_2 - G_2^+]$  are the spectral functions for the isolated contacts 1 and 2 respectively. We define,

$$\{S\} \equiv \tau_1 \{\Phi_1\} + \tau_2 \{\Phi_2\}$$

is the sum of the source terms  $\tau_1 \Phi_1$  (from the source) and  $\tau_2 \Phi_2$  (from the drain). The channel Green's function will be given by

$$G \equiv [EI - H - \Sigma_1 - \Sigma_2]^{-1} \quad (4.11)$$

and use it to express the channel wavefunction in terms of the source terms from Eq. 4.10:

$$\{\psi\} = G\{S\} \rightarrow \{\psi\}\{\psi\}^+ = G\{S\}\{S\}^+G^+$$

### 4.1.2 Green's function calculation

We used our own transport code to compute surface green's function and channel green's function, hence transmission function. Here and in next section, I will explain how the code works.

We begin with the time indepedent Schrödinger equation,

$$[H_0(\mathbf{r}) - E] \psi(\mathbf{r}) = 0$$

The green's function corresponding to the equation will be,

$$[H_0(\mathbf{r}) - E] G_0(\mathbf{r}, \mathbf{r}', E) = -\delta(\mathbf{r} - \mathbf{r}')$$

The reason for which we introduce Green's function is to be able to solve inhomogeneous equation from the known solutions of the corresponding homogeneous equation. If we have a inhomogeneous equation of the form:

$$[H_0(\mathbf{r}) - E] \psi(\mathbf{r}) = S(\mathbf{r})$$

where  $S(\mathbf{r})$  is a known function (source term), then  $\psi(\mathbf{r})$  can be shown to be obtained as

$$\psi(\mathbf{r}) = - \int S(\mathbf{r}') G_0(\mathbf{r}, \mathbf{r}', E) d\mathbf{r}' \quad (4.12)$$

If,

$$S(\mathbf{r}) = -\tau(\mathbf{r})\psi(\mathbf{r})$$

then the solution to Eq. 4.12 becomes,

$$\psi(\mathbf{r}) = \psi_0(\mathbf{r}) + \int G_0(\mathbf{r}, \mathbf{r}', E) \tau(\mathbf{r}') \psi(\mathbf{r}') d\mathbf{r}'$$

which points at a recursive approach which results into an expansion in the order of  $\tau$  upon successive recursion,

$$\begin{aligned} \psi &= \psi_0 + G_0 \tau \psi_0 + G_0 \tau G_0 V \psi_0 + G_0 \tau G_0 \tau G_0 \tau \psi_0 + \dots \\ &= \psi_0 + (G_0 + G_0 \tau G_0 + G_0 \tau G_0 \tau G_0 + \dots) \tau \psi_0 \end{aligned}$$

Hence, it allows us write a net  $G$  as:

$$\begin{aligned} G &= G_0 + G_0 \tau G_0 + G_0 \tau G_0 \tau G_0 + \dots \\ &= G_0 + G_0 \tau (G_0 + G_0 \tau G_0 + \dots) \end{aligned}$$

Hence gives,

$$G = G_0 + G_0 \tau G \quad (4.13)$$

Here,  $\tau$  is hoping or coupling term.

### 4.1.3 Green's function convergence

It is known that any surface can be viewed as an semi-infinite stack of principal layers with nearest-neighbor interactions.[11] This corresponds to transforming the original system into a linear chain of principal layers.

The code converges  $G$  for the surface layer of electrode i.e the "zeroth" layer. All the principal layers isolated will have the same green's function,  $G_0$ . It starts from the zeroth level, and couples to the next principal layer, the change in green's function is governed by eq (4.13). The following goes on untill converge condition is satisfied. It follows the following schematic (pli means principal layer i),

- Takes an isolated layer (pl0) constructed  $G_0$ . All such pl layers in isolation has same  $G_0$ .

- It couples  $G_0(\text{pl1})$  to  $G(\text{pl0})$ , which as a result it changes from  $G_0$  to say  $G_1$
- Next  $G_0(\text{pl2})$  is coupled to  $G_0(\text{pl1})$ ,  $G_0$  changes to  $G_1$  and  $G_1$  is coupled  $G_1(\text{pl0})$  to change it  $G_2$
- It goes on until the change in  $G$  is very small

The principal layers does not require to be explicitly built, the only requirement is  $G_0$  and  $\tau$ .

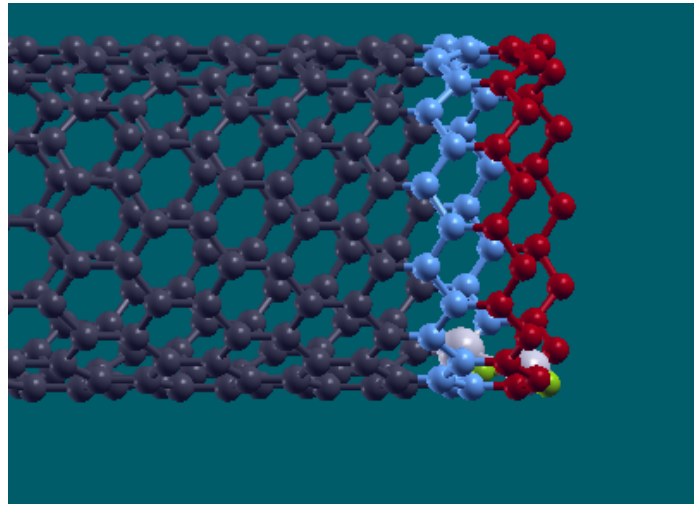


Figure 4.3: Two principal layers constructed at an edge of CNT

#### 4.1.4 Zero bias transport

We have derived enough results to compute the non-equilibrium density matrix, now we will move to current, electronic transport. Again, we will start with the one-contact problem.

We write the homogeneous Schrödinger equation ( $S_R=0$  and  $\Phi = \Phi_R + \chi$ ) in one-contact problem,

$$E \begin{Bmatrix} \psi \\ \Phi \end{Bmatrix} = \begin{bmatrix} H & \tau \\ \tau^+ & H_R - i\eta \end{bmatrix} \begin{Bmatrix} \psi \\ \Phi \end{Bmatrix}$$

To calculate current flow, we need to look at the time-dependent version of this equation,

$$i\hbar \frac{d}{dt} \begin{Bmatrix} \psi \\ \Phi \end{Bmatrix} = \begin{bmatrix} H & \tau \\ \tau^+ & H_R - i\eta \end{bmatrix} \begin{Bmatrix} \psi \\ \Phi \end{Bmatrix}$$

and obtain an expression for the time rate of change in the probability density inside the channel, which is given by  $\text{Tr} [\psi\psi^+] = \text{Tr} [\psi^+\psi] = \psi^+\psi$

$$I \equiv \frac{d}{dt} \psi^+\psi = \frac{\text{Trace} [\psi^+\tau\Phi - \Phi^+\tau^+\psi]}{i\hbar}$$

We know that  $\{\Phi\} \equiv \{\Phi_R + \chi\}$ , hence we can divide this net current  $I$  conceptually into an inflow part which is proportional to the incident wave  $\{\Phi_R\}$ , and an outflow part proportional to the scattered wave  $\{\chi\}$  :

$$I = \underbrace{\frac{\text{Trace} [\psi^+\tau\Phi_R - \Phi_R^+\tau^+\psi]}{i\hbar}}_{\text{Inflow}} - \underbrace{\frac{\text{Trace} [\chi^+\tau^+\psi - \psi^+\tau\chi]}{i\hbar}}_{\text{Outflow}} \quad (4.14)$$

Making use of Eqs. (4.2) and (4.3), we can write the inflow as, (since  $[A] = i[G - G^+]$ )  
 $\text{Inflow} = \text{Trace} [S^+G^+S - S^+GS] / i\hbar = \text{Trace} [SS^+A] / \hbar$

To obtain the total inflow, we need to integrate the inflow due to each contact eigen-state  $\alpha$ , that is all energy. So, after further calculations,

$$\text{Inflow} = \frac{1}{\hbar} \int \frac{dE}{2\pi} f_0(E - \mu) \text{Trace}[\Gamma A] \quad (4.15)$$

where  $f_0$  is the fermi function and  $\mu$  is the chemical potential of the fermi level. Now for outflow, using Eqs. (4.1), (4.14) and  $\Gamma = i[\Sigma - \Sigma^+]$ ,

$\text{Outflow} = \text{Trace} [\psi\psi^+\Gamma] / \hbar$  Integrating over  $E$  and further calculations gives,

$$\text{Outflow} = \frac{1}{\hbar} \int \frac{dE}{2\pi} \text{Trace}[\Gamma G^n] \quad (4.16)$$

Going to two contact scenario,

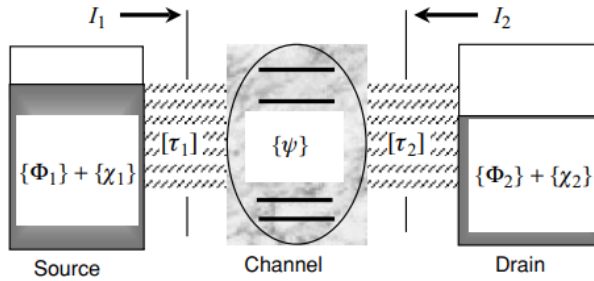


Figure 4.4: Inflow and outflow at the contacts[1]

The outflow and inflow for  $i$ th contact will be ( $i = 1$  or  $2$ ),

$$\text{Infl}_i = \frac{1}{\hbar} \int \frac{dE}{2\pi} f_i \text{Trace}[\Gamma_i A] \quad (4.17)$$

$$\text{Outfl}_i = \frac{1}{\hbar} \int \frac{dE}{2\pi} \text{Trace}[\Gamma_i G^n] \quad (4.18)$$

Hence, the net current  $I_i$  (at  $i$ th contact) is given by the difference between the inflow and the outflow (multiplied by the charge of an electron),

$$I_i = (-q/\hbar) \int_{-\infty}^{+\infty} \frac{dE}{2\pi} \tilde{I}_i(E) \quad (4.19)$$

where,

$\tilde{I}_i = \text{Trace}[\Gamma_i A] f_i - \text{Trace}[\Gamma_i G^n]$  and  $A$  is the total spectral function ( $A_1 + A_2$ ).

#### 4.1.5 Zero bias Transmission function

Using Eqs. (4.11) and  $A = A_1 + A_2$  in Eq (4.19),

$$\begin{aligned} \bar{I}_1 &= \bar{T}_{12}(E) [f_1(E) - f_2(E)] && \text{where } \bar{T}_{12}(E) \equiv \text{Trace}[\Gamma_1 A_2] \\ \bar{I}_2 &= \bar{T}_{21}(E) [f_2(E) - f_1(E)] && \text{where } \bar{T}_{21}(E) \equiv \text{Trace}[\Gamma_2 A_1] \end{aligned}$$

We expect the currents at the two terminals to be equal and opposite and this is ensured if  $\text{Trace}[\Gamma_1 A_2] = \text{Trace}[\Gamma_2 A_1]$ , which is the case of zero bias. We can show that mathematically using the Eq. (4.7) in above equations.

This leads to writing the current as,

$$I = (q/h) \int_{-\infty}^{+\infty} dE \bar{T}(E) [f_1(E) - f_2(E)]$$

where

$$\begin{aligned} \bar{T}(E) &\equiv \text{Trace} [\Gamma_1 A_2] = \text{Trace} [\Gamma_2 A_1] \\ &= \text{Trace} [\Gamma_1 G \Gamma_2 G^+] = \text{Trace} [\Gamma_2 G \Gamma_1 G^+] \end{aligned}$$

This  $\bar{T}(E)$  is called the transmission function. Physically, we can view the transmission function  $\bar{T}(E)$  as a measure of probability of electrons with energy  $E$  that it can pass through the channel.

## 4.2 Results

### 4.2.1 Transmission function in MS and SS heterojunctions

We studied the electronic properties of many Metal-Semiconductor (MS) and Semiconductor-Semiconductor (SS) heterojunctions. As we have seen in section 3.4.2, we found that there are **defect states** near fermi-level, which can act as channels for electronic transport. Plotting of the zero-bias transmission function (calculated from the green's function) and DOS (calculated from the spectral function), revealed a transmission gap, few of those have defect states in the gap region. *This confirms that the defect states near Fermi level do not contribute to transmission when there is no bias, therefore they are isolated.*

**Red plot is the Density of states (DOS) graph and Blue plot is Transmission function T(E) graph.** The defects are mentioned in the captions.

### MS heterojunctions:

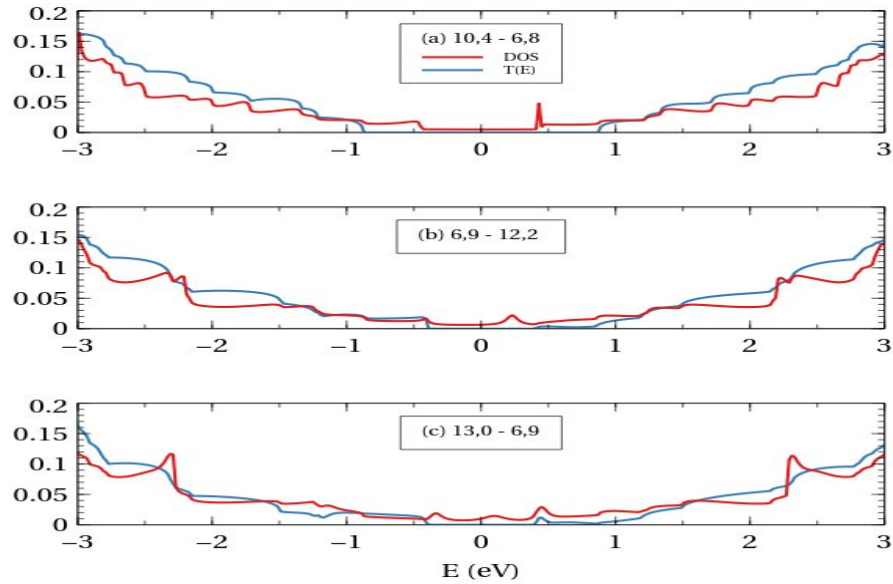


Figure 4.5: (a) 10,4-6,8 (2A type) (b) 6,9-12,2 (2A+1B type) (c) 13,0-6,9 (2A+2B type)

### SS heterojunctions:

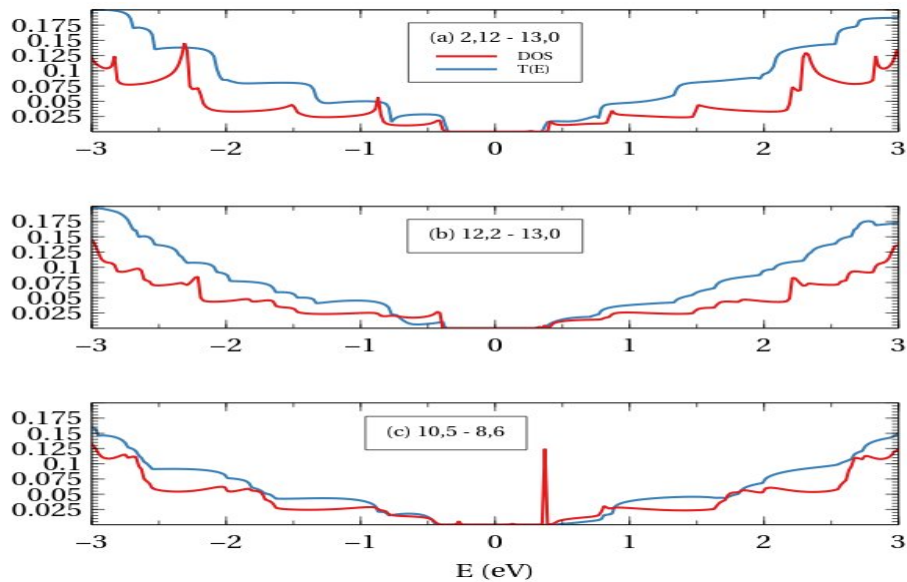


Figure 4.6: (a) 2,12-13,0 (1B type) (b) 12,2-5,10 (1A+1B type) (c) 10,5-8,6 (2A+1B type)

Here, for MS (10,4-6,8) and SS (10,5-8,6), we can see peaks in DOS, in transmission gap region. We claim that the peaks are from the defect states, as the pristine tubes will give a gap in DOS near fermi level. This defects can provide channel states for transport upon applying some bias voltage. Hence, they can be used as ON/OFF devices and will have other diode applications. MS heterojunctions will require lesser voltage to switch ON, as they have other states too (from the metal part) in the gap region.

#### 4.2.2 Isolated defect states

The above results suggested that there might be some correlation between number of defects, defect spacing and defect peaks in transmission gaps. Hence we set out on an extensive search in SS heterojunctions, with varying defect arrangements and radius of CNT-HJs.

**Left images show the defect arrangements at the interface of the tubes, Right images show the DOS and transmission plots (Red plot is the Density of states (DOS) graph and Blue plot is Transmission function  $T(E)$  graph).**

**Defects : 2 A type**

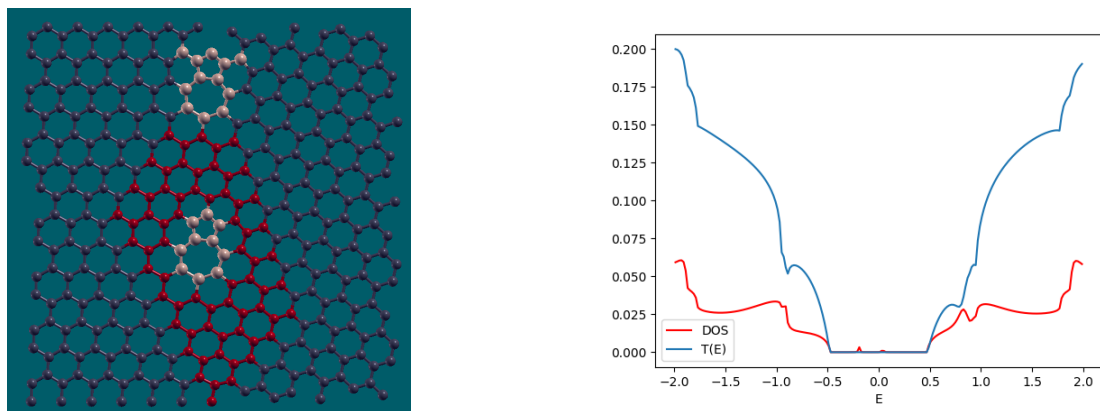


Figure 4.7: 6,7 - 9,4 ; Radius = 4 Ang.

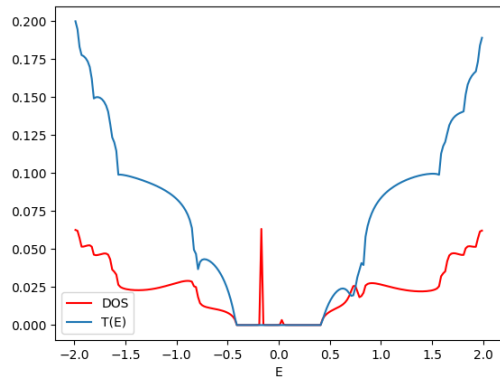
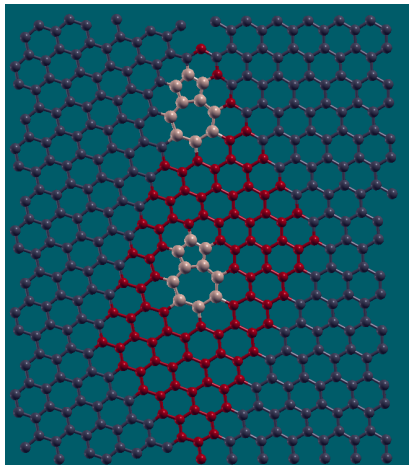


Figure 4.8: 10,5 - 7,8 ; Radius = 5 Ang.

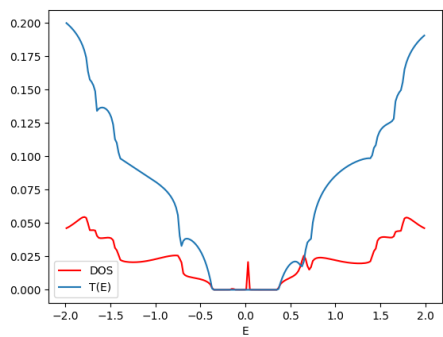
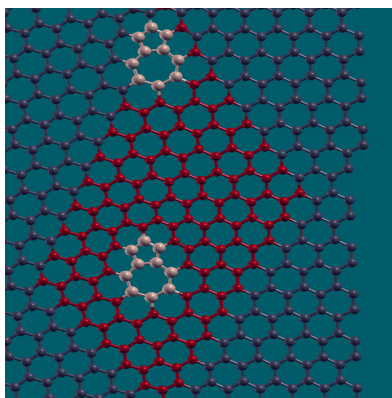


Figure 4.9: 11,6 - 8,9 ; Radius = 6 Ang.

Defects : 3 A type

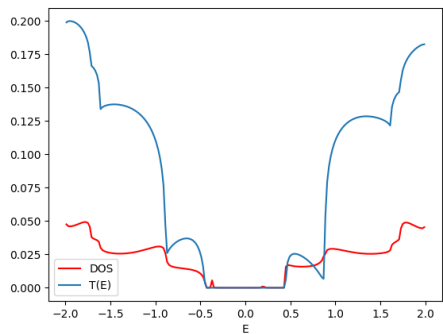
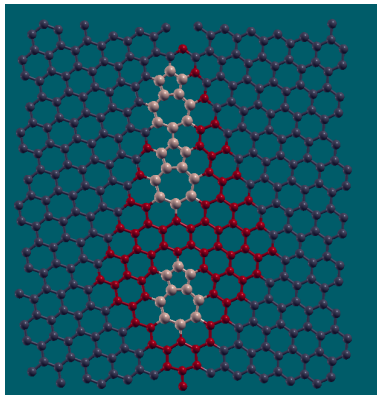


Figure 4.10: 9,5 - 8,6 ; Radius = 5 Ang.

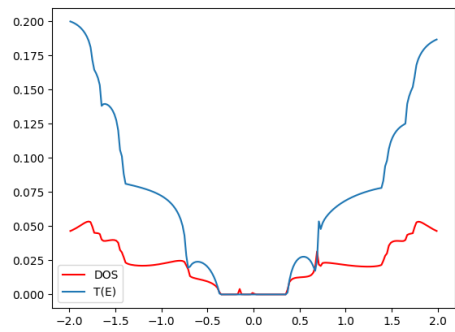
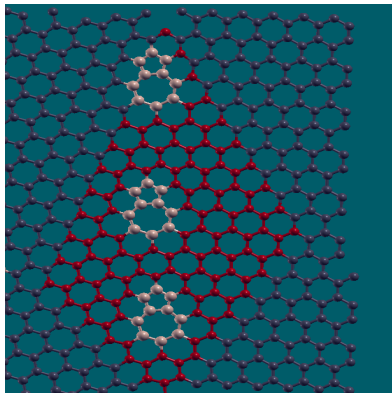


Figure 4.11: 11,6 - 9,8 ; Radius = 6 Ang.

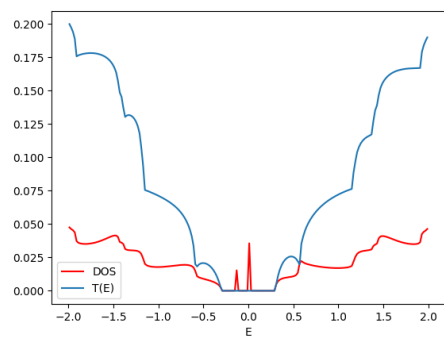
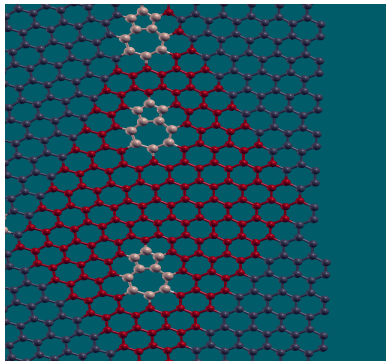


Figure 4.12: 13,8 - 11,10 ; Radius = 7 Ang.

Defects : 4 A type

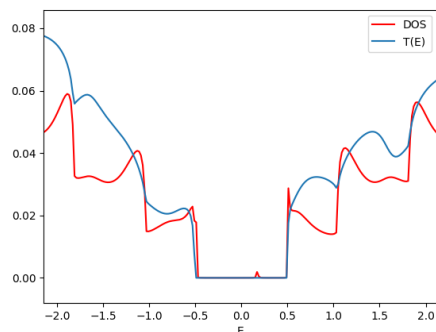
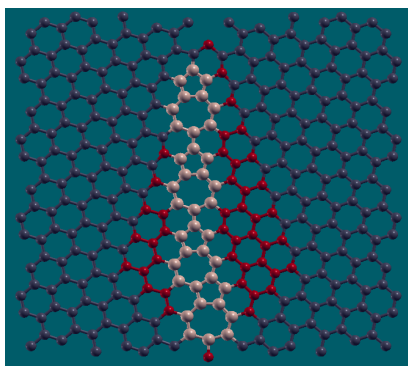


Figure 4.13: 8,4 - 8,4 ; Radius = 4 Ang.

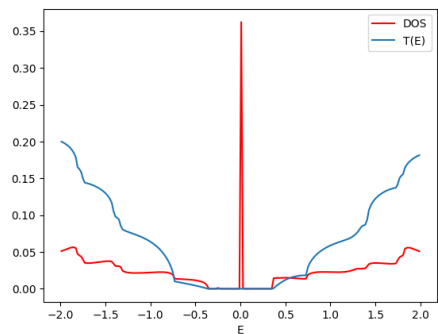
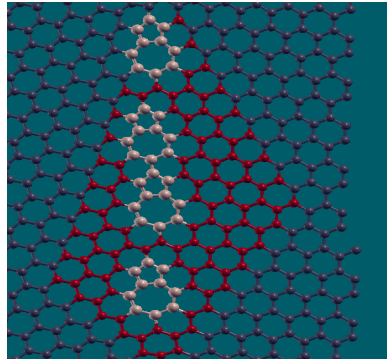


Figure 4.14: 12,5 - 9,8 ; Radius = 6 Ang.

**Defects : 5 A type**

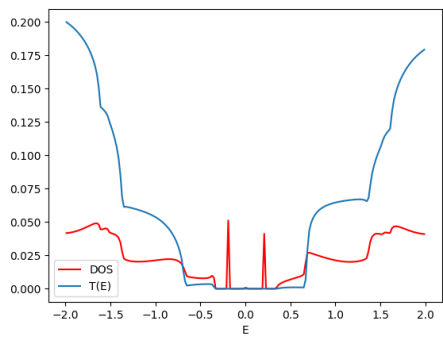
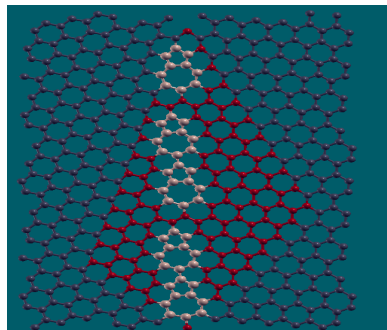


Figure 4.15: 13,5 - 10,8 ; Radius = 6 Ang.

**Defects : 2 A + 1 B type**

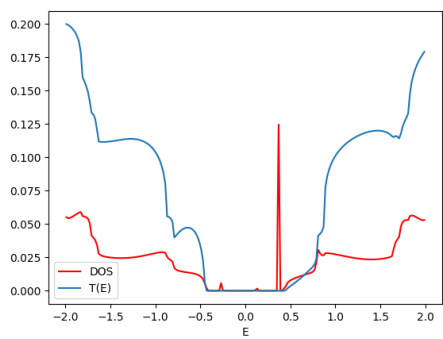
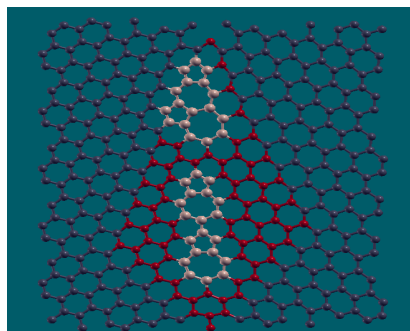


Figure 4.16: 10,5 - 8,6 ; Radius = 5 Ang.



Figure 4.17: 14,3 - 7,11 ; Radius = 6 Ang.

The appearance of isolated defect states peaks seem to have a correlation with the number of defects and their arrangement on the interface of the heterojunction. To start with SS heterojunctions, we had 10,5-8,6 (2A+1B type). So we began by removing the B defect and varying the radius. At 5 ang. radius, we got a peak in transmission gap (T gap). For lower or higher radius (4 ang. or 5 ang.), the defect states delocalize hence we lose the peak. It suggests that there might be an optimum A to A separation that gives localization in the defect peak.

We move on to 3A and 4A defects. In 3A type, the optimum radius is 7 ang. where it gives small two peaks. In 4A type, the optimum defect separation is achieved at radius 6 ang where the defects are distributed most evenly, hence shows localization. In 5A type, the peak is seen again in 6 ang radius.

We came back to our 10,5-8,6 HJ which had 2A and 1B defects, which showed localization. Adding more A type or B defect, or increasing the radius loses the peak from the T gap.

It is clear from the plots and interface diagrams that the defect states being present in the T gap does not only depend on the number of defects or radius, but also the arrangement in which they are present in the junction region. With each optimum radius and defect arrangement, we can suggest more such CNT-HJs which will give

defect peaks in the transmission gap region.

It might seem like we can build a rectifying device out of these heterojunctions (those favours peaks at the fermi level). But the energetics of both the carbon nanotubes that make up the HJ, are same or similar. This is due to the fact that both the tubes are made up of same element, carbon. We took an example of SS heterojunction (10,5-7,8) to demonstrate this. In the plot below, we compared DOS of pristine 10,5 and 7,8 tubes (the plot of 10,5-7,8 is given as reference).

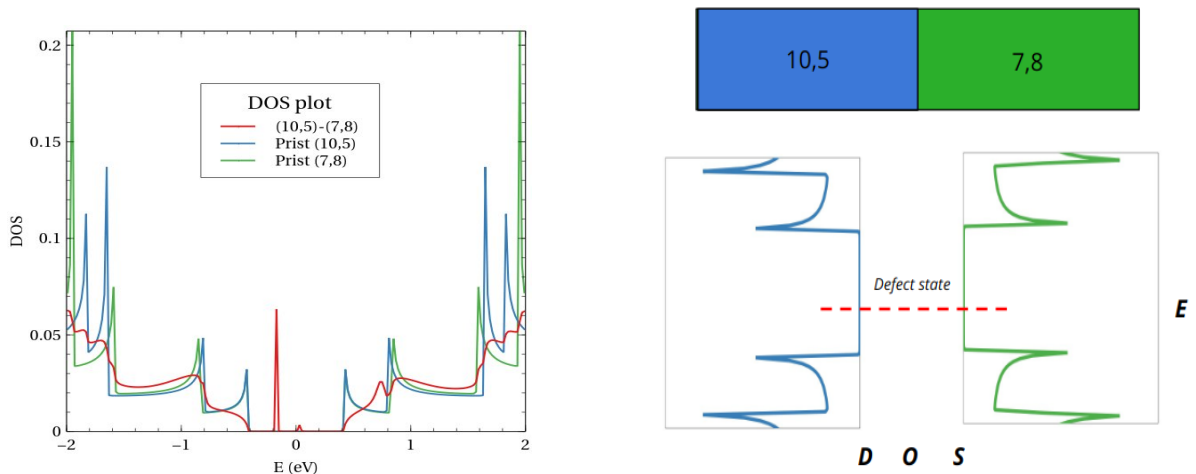


Figure 4.18: DOS of pristine tubes and the heterojunction (10,5-7,8)

As we can see in the above figure (right), the DOS of 10,5 and 7,8 tubes are almost the same and the defect state lie somewhere in between. If we apply positive bias, the left DOS will shift up and right will shift down, the defect state(red line) will start helping in transport once it finds states on both sides. In case of negative bias, the left DOS shifts down and the right one shifts up, and the defect states will conduct again. We can observe that the positive bias required for conductance is almost same as negative bias. Hence we cannot build a rectifier out of this heterojunction, but can be used as an ON/OFF device. We can bring a shift in the DOS by doping nitrogen(N) on one side and boron(B) on the other, thus bringing a rectifying nature.

# Chapter 5

## Conclusion

**Linear shapes are preferred in device applications.** This was the motivation behind our relaxation study on CNT-HJs. We have found that 2 A states (and other examples) uniformly spaced, balances each other and have a very less bending angle  $\phi$ .

We started our search for magnetic or active materials that can be used for various application purposes like memory device, switch etc. We can make such heterostructures by introducing simple topological defects which break the bipartite nature. Correlation between defects (with length) and magnetism has also been studied, which showed some promise. Now, further studies have to be done to conclude on the possibilities of such magnetic materials to be tuned and functional.

Then we studied PDOS of regions of CNT-HJs and found quite a few structures which have such defect states, suggesting active nature. This led to an extensive transport study of such CNT-HJs. A few CNT-HJs are found to have defect states in gap region. These defect states will help as a channel for electronic transport, upon applying a bias voltage, making it a diode-like device.

After merging both of these searches, 2 A defect and 4 A type SS heterojunctions seemed to have shown some promise. In the heterojunctions, uniformly distributed 2A defects perfectly balance each other, making it linear and on the other hand also shows diode-like properties for certain AA separations (related to radius).

Our goal is to make MSSM junctions with both active and passive elements, from the CNTs as shown below.

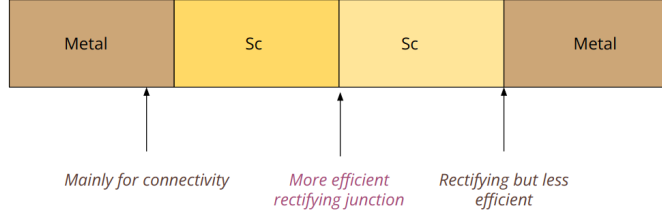


Figure 5.1: Device applications of linear MS and SS heterojunctions

This brings us to the conclusion, of what further changes can be made and what are our future goals,

1. **Curvature effects:** Our TB framework considered only  $\pi$  electrons for the calculations i.e the  $P_z$  electrons, which does not exist in pure form due to curvature effects of CNT. It exists as a hybridisation close to  $sp^3$  but not exactly, a state called  $sp^3s^*$  [12]. Our next goal would use another framework which utilises DFT to calculate tight binding parameters for the given system, hence gives us more of a practical picture. Then we can study radius dependence on the various properties, and also find projected DOS of wave functions to get a greater depth on the density of states of the heterojunction.
2. Expanding the search to more CNT-HJs.
3. To do transport calculations on relaxed CNT-HJs with next nearest and next-nearest hoping / interaction.
4. Transport study on doped carbon nanotube heterojunction (doping nitrogen(N) on one side and boron(B) on the other side).
5. To do a conductance study with bias voltage.
6. Thermal transport study.

# References

- [1] S. Datta, *Quantum transport: atom to transistor.* Cambridge university press, 2005.
- [2] S. Iijima, “Helical microtubules of graphitic carbon,” *Nature*, 1991.
- [3] H. Kim, J. Lee, S.-J. Kahng, Y.-W. Son, S. Lee, C.-K. Lee, J. Ihm, and Y. Kuk, “Direct observation of localized defect states in semiconductor nanotube junctions,” *Physical review letters*, vol. 90, no. 21, p. 216107, 2003.
- [4] B. I. Dunlap, “Relating carbon tubules,” *Physical Review B*, vol. 49, no. 8, p. 5643, 1994.
- [5] Y. Yao, Q. Li, J. Zhang, R. Liu, L. Jiao, Y. T. Zhu, and Z. Liu, “Temperature-mediated growth of single-walled carbon-nanotube intramolecular junctions,” *Nature materials*, vol. 6, no. 4, pp. 283–286, 2007.
- [6] C. Jin, K. Suenaga, and S. Iijima, “Plumbing carbon nanotubes,” *Nature Nanotechnology*, vol. 3, no. 1, pp. 17–21, 2008.
- [7] J. Bhattacharjee and J. Neaton, “Interfacing carbon nanotubes of arbitrary chiralities into linear heterojunctions,” *Physical Review B*, vol. 83, no. 16, p. 165432, 2011.
- [8] D. W. Brenner, “Empirical potential for hydrocarbons for use in simulating the chemical vapor deposition of diamond films,” *Physical review B*, vol. 42, no. 15, p. 9458, 1990.

---

*REFERENCES*

- [9] Z. Mao, A. Garg, and S. B. Sinnott, “Molecular dynamics simulations of the filling and decorating of carbon nanotubules,” *Nanotechnology*, vol. 10, no. 3, p. 273, 1999.
- [10] J. Hubbard, “Electron correlations in narrow energy bands,” *Proceedings of the Royal Society of London. Series A. Mathematical and Physical Sciences*, vol. 276, no. 1365, pp. 238–257, 1963.
- [11] D. Lee and J. Joannopoulos, “Simple scheme for surface-band calculations. ii. the green’s function,” *Physical Review B*, vol. 23, no. 10, p. 4997, 1981.
- [12] J. X. Cao, X. H. Yan, J. W. Ding, D. L. Wang, and D. Lu, “Electronic properties of single-walled carbon nanotubes,” *Journal of the Physical Society of Japan*, vol. 71, no. 5, pp. 1339–1345, 2002.